Cool down of subsea dead-leg with a cold spot

Experimental and numerical heat transfer analysis

by

Ola Hagemann

THESIS
for degree of
MASTER OF SCIENCE

(Master i Anvendt matematikk og mekanikk)

Faculty of Mathematics and Natural Sciences
University of Oslo

November 2014

Det matematisk- naturvitenskapelige fakultet
Universitetet i Oslo

Abstract

In a subsea facility, the pipelines will be surrounded by sea water at $4°C$, which will actively cool the production fluid inside. If temperatures drop below a critical value, water and gas will form unwanted solids called hydrates. Dead legs are inactive parts of production pipelines occupied by stagnant hydrocarbons. These areas pose a major hydrate formation risk, and needs to be insulated based on a prior heat transfer analysis. If a dead leg contains access points for e.g remotely operated vehicles, these areas need to be kept uninsulated, and will act as cold spots. Due to internal natural convection, these cold spots will potentially influence the temperatures throughout the system, and it is therefore crucial to predict the degree of influence. In this master thesis, experimental and numerical heat transfer analysis was conducted on a T-shaped plexiglass pipe, representing a production header with a vertical dead-leg. The header was insulated, while the dead-leg was uninsulated and carried a cold spot on top. In the first of two experimental phases, water was circulated through the header at constant flow rate, mimicking steady state production. In the second phase, the flow was enclosed and the water was cooled down over a period of 3 hours. During both phases, internal and external temperatures were measured with RTD's and thermocouples respectively, while velocities in the dead leg were measured using PIV. It was shown how the mean velocity field rotated periodically in a clockwise and counter-clockwise manner during both phases. A numerical model was created in Workbench, and simulations were carried out using RANS with a $k-\omega$ SST formulation in CFX. Temperatures were correctly predicted for 3 hours of cool down, by modelling the cold spot as an isothermal wall, even though simulations failed to recreate the periodic mean velocity field observed in the experiment.

Acknowledgements

First of all, I would like to thank my main supervisor Atle Jensen for experimental guidance and fruitful discussions. Many thanks are also directed towards my second supervisor, Mikael Mortensen, for helping me with the numerical analysis. I would also like to thank my external supervisor Stig Grafsrønningen for an introduction on performing cool down experiments, and help with creating a numerical model.

As most master students, I had limited lab experience, and setting up an experiment with so many components involved would not have been possible without the lab engineer at the "Hydrodynamic Wave lab" at UiO, Olav Gundersen. He has provided technical guidance, as well as help with setting up the experiment and designing the aluminium cold spot. I would also like to thank Trine Jelstad Olsen for help with fixing my numerical model when I could not figure out what made the meshing process fail over and over again, Jostein Kolaas for setting up the laser, and Bjørn Frostmann at Armacell for providing me with complimentary Armaflex insulation.

Being surrounded by motivating master and Ph.D. students has also been very beneficial, and I would especially like to thank Anis Awal Ayati for his useful advice and feedback. Last but not least, I would like to thank my family and my girlfriend Isabell B. Johansen for supporting and motivating me.

Contents

Nomenclature

α	Thermal diffusivity
ϵ	Dissipation
μ	Dynamic viscosity
ν	Kinematic viscosity
ρ	Density
$\mathbf{g}$	Gravity
$\mathbf{u}$	Velocity
k	Turbulent Kinetic Energy
p	Pressure
Ra	Rayleigh number $Ra = \frac{g\beta\Delta T L^3}{\alpha\nu}$
T_0	Reference temperature
LDA	Lased Doppler Anemometry
LES	Large Eddy Simulation
CAD	Computer Aided Design
CFD	Computational Fluid Dynamics
PVT	Pressure Volume Temperature
RANS	Reynolds Averaged Navier-Stokes

Chapter 1

Introduction

1.1 Introduction

When designing a subsea facility, the main goal is to optimize production, while keeping expenses at a minimum. This is very difficult when producing at the high pressures and low temperatures present at the sea floor. Under these conditions, water and gas have a tendency to form solid crystals called hydrates. These solids will cause erosion and clogging of production pipelines, limiting its lifetime and productivity. It is therefore necessary to insulate some areas of the pipeline, to avoid hydrate formation. Optimal insulation design requires a prior thermal analysis, which is usually carried out through Finite Element Analysis. However, if ROV(Remotely Operated Vehicles) access points are required, they need to be kept uninsulated, acting as cold spots(Janoff et al. [2004]). Cold spots will trigger the onset of natural convection, which will be the main heat transfer mechanism when the facility is not producing(e.g shut down). Natural convection is also important in dead-legs, which are inactive branches of a production pipeline occupied by stagnant fluid, because temperatures in these branches are lower than in the producing ones. To include heat transfer due to natural convection in a thermal analysis, Computational Fluid Dynamics(CFD) is required. The results obtained from a CFD analysis needs to be validated against experimental data. In a full scale experiment, a subsea component made of e.g steel, is equipped with thermocouples and lowered into a pool of cold water. Temperatures are measured during two phases; steady state circulation of warm water through the components interior, and a consequent cool down where the warm water is enclosed. The validation of the numerical model is based solely on its ability to predict the temperature evolution, even though e.g velocities might be wrong. To evaluate the numerical flow kinematics, one also need data on the experimental velocity field, which is hard to measure

through the walls of a steel pipe.

1.1.1 Litterature review

In this literature review, important research on flow kinematics of internal natural convection is introduced. The research papers differ in terms of experimental geometry, measurement technique, and industrial relevance. Natural convection in cavities of different geometries have been widely studied due to its simplicity, and the result have been used to validate and improve numerical CFD models. Low-turbulence natural convection was studied by Tian and Karayiannis [2000] for a square cavity at $Ra = 1.58e^9$, obtained through differentially heating two vertical walls. The flow was turbulent anisotropic wall shear flow, and it was found that the fluctuating velocity components were independent of each other. The study reported root mean square values for temperatures and velocities; $T'_{rms}, u'_{rms}, v'_{rms}$, and Reynolds stress, measured with a 2D LDA, and thermocouples. The same year, Betts and Bokhari [2000] performed similar experimental studies on a rectangular cavity where the reduced width yielded $Ra = 1.46e^6$ for almost the same temperature differential. The flow in the core of the cavity was found to be fully turbulent, but both temperature and flow field were found to be closely two dimensional in most parts of the cavity. Both of these studies provide scientists with excellent benchmark data for evaluating whether numerical models are able to correctly predict the turbulence in natural convective flow. The author of this thesis attempted to evaluate the flow kinematics described in Tian and Karayiannis [2000] using $k - \omega$ SST in CFX. This was considered an introduction to understanding the difficulties with modelling flow which is both turbulent(close to the wall) and laminar(far from the wall) at the same time. Attempting to solve the case with a steady state solver, resulted in relaminarization. However, the differences between the experimental and numerical vertical velocity were small, despite the numerical flow being laminar.

Many research papers focus on natural convection in pipelines, due to its industrial relevance. Natural convection in high Rayleigh number flows was investigated by Bejan and Kimura [1980] in horizontal pipes with different end temperatures. A cylindrical cavity with a diameter to length ratio of $D/L = 0.112$, was heated at one end and cooled at the other obtaining Rayleigh numbers in the range: $10^8 < Ra < 10^{10}$. Thymol blue method in a combination with thermocouples was used for measuring velocities and temperatures. Temperature varied linearly with depth in the mid section, occupied by stagnant water. A warm and cold water jet gave steep temperature gradients along the top and bottom of the pipe respectively, and

velocities were higher in the warm jet. For vertical pipe flow at high Rayleigh numbers,Yan and Lin [1991] found that the flow behaviour approached that of flow along a vertical flat plate. At low Ra the pipe curvature had a strong influence on flow behaviour. Measurements in this study was limited to temperatures from pipe-wall mounted thermocouples.

Only a handful of published papers were found for flow in dead-legs, probably due to most of them being confidential. Stagnant fluid in horizontal dead-legs of different D/L ratios was investigated by Habib et al. [2005] both numerically and experimentally. A fluid mixture of 90% crude oil and 10% water by volume, was circulated at steady state through a T-shaped pipe, where one horizontal end was inactive. It was shown that dead-leg length and inlet flow velocity had an effect on oil/water separation, which is a trigger for hydrate formation. These results were validated against flow visualization experiments.

Available research on natural convection caused by cold spots was also very limited. Recent studies by Mme [2010] investigated the effect of cold spots on temperatures in a water filled steel pipe. The cold spot was created by circulating water around a copper ring attached to the steel pipe. The cooling effect was found to be largest when the pipe was horizontal. Experimental results were compared with numerical results obtained with CFD computations, and showed that LES was better suited than $k - \epsilon$ based models. However, experimental temperature data was obtained solely for the pipe wall, and the CFD velocity data was not validated.

The starting point for this thesis was a previous study by Grafsrønningen and Jensen [2014], where cool down experiments over 3 hours was conducted on a water filled T-shaped plexiglass pipe, representing a production header with a vertical dead-leg. The header was insulated, while the dead-leg was kept uninsulated. Temperatures throughout the T-pipe was measured internally with RTD's and externally with pipe-wall mounted thermocouples, while velocity data was obtained in the dead-leg only. It was shown that cool down simulations were more sensitive to mesh design than choice of turbulence model. Mesh independent results were obtained by running a series of mesh convergence tests. The thermal field was correctly predicted with a RANS model for the entire cool down, even though the flow was laminar after 60 minutes. Velocities in the dead-leg coincided well with experimental PIV data during the first 60 minutes, but RANS was not able to predict laminar flow kinematics. In the present study, the experiment was modified with a cold spot on top of the dead-leg, and a more uniform insulation on the header. These modifications were also made in the numerical geometry, and

a mesh was created based on the recommendations given by Grafsrønningen and Jensen [2014] in Workbench. The cold spot was believed to increase the cooling effect, due to a larger internal temperature gradient, which is the driving force for natural convection. In this master thesis, the main goals were:

- Obtain experimental velocity and temperature data of high quality
- Use this data to validate a numerical model created in ANSYS CFX

Based on this literature review, there has not yet been any published results on experimental validation of a transient CFD model including a dead-leg and a cold spot, in terms of both kinematic and thermal flow fields.

Chapter 2

Heat transfer and Turbulence Modelling

2.1 Internal natural convection

Avoiding hydrate formation in subsea pipelines requires thorough thermal analysis, so that the proper insulation can be designed. It is also necessary to evaluate what influence local effects from dead-legs and cold spots might have on temperatures throughout the rest of the pipe. Heat exchange due to fluid movement inside the pipeline, pose a major hydrate formation risk during shut-down. Together with conservation equations for mass and energy, the movement of a fluid is governed by the Navier-Stokes equations. Water is a fluid that is considered incompressible in terms of pressure and temperature, which means that both density and viscosity are constant. The incompressible Navier-Stokes and Continuity equation is given below in Eq. (2.1) and (2.2)

$$\rho\left(\frac{\partial \mathbf{u}}{\partial t} + (\mathbf{u}\cdot\nabla)\,\mathbf{u}\right) = -\nabla p + \rho\mathbf{g} + \mu\nabla^2\mathbf{u} \tag{2.1}$$

$$\nabla\cdot\mathbf{u} = 0 \tag{2.2}$$

Incompressibility is a good assumption in many types of flow, but not in the presence of large temperature gradients. Under these conditions density differences will cause a gravity driven circulation known as natural convection. Boussinesq suggested (White [2006]) that incompressibility was a good assumption for all terms in equation (2.1) except for the term where ρ is multiplied with g,and that ρ in this term should be approximated as;

$$\rho' \approx \rho\,(1 - \beta\,(T - T_0)) \tag{2.3}$$

stating that it varies with the change in temperature T and thermal expansion coefficient β. In order to solve equation (2.1) - (2.2) a transport equation for the temperature is required. The incompressible heat equation is given as:

$$\rho C_p \left(\frac{\partial T}{\partial t} + \mathbf{u} \cdot \nabla T \right) = \nabla \cdot (k \nabla T) \tag{2.4}$$

In equation (2.4), C_p is the heat capacity, and k is the thermal conductivity.

Due to the non-linear convective terms in equation (2.1) and (2.4), it is not possible to obtain an analytical solution to a "real-life" thermal analysis, making scientists reliant on numerical models. Numerical models need to be validated through the use of experimental data. Designing and performing experiments on pipelines with the relevant dimensions can be a time consuming and expensive process. It is therefore very important to make experimental datasets useful for validation of numerical models with similar geometry under similar conditions. Dimensionless analysis is a way of categorizing the important parameters in a specific flow problem.

2.1.1 Dimensionless analysis

The starting point for non-dimensionalizing the Navier-Stokes equations is to find what the characteristic flow properties are. When a pressure differential drives a fluid through a horizontal pipeline, the characteristic length is the pipe diameter(D), while the bulk velocity is the characteristic velocity scale(U). Dividing a variable with its characteristic scale, makes the variable non-dimensional. Replacing all the variables in equation (2.1) with its dimensionless counterpart, gives the equation on its non-dimensional form. By simplifying and rearranging this equation, the very important dimensionless Reynolds number, $Re = (UL)/\nu$, is revealed. It is multiplied as $1/Re$ with the viscous term in equation (2.1), making viscous effects negligible in high Reynolds number flow. Transition from laminar to turbulent flow has been shown to happen at $Re > 2000$. The Reynolds number serves as a common factor, enabling comparison of experimental and numerical data obtained with slightly different geometries but with equal Reynolds numbers.

In natural convective flow the velocity is induced by gravity acting on density differences, and the characteristic velocity scale is often set to $\sqrt{g\beta(T_w - T_0)L}$ (White [2006]). Dimensional analysis with the use of this characteristic velocity reveals the dimensionless Grashof number. It is in analogy with Re multiplied with the viscous term, but as $1/\sqrt{Gr}$. Viscous effects can there-

fore be considered negligible also at high Gr numbers.

$$Gr = \frac{g\beta\rho^2 L^3(T_w - T_0)}{\mu^2} \tag{2.5}$$

If dealing with flow along a vertical wall, the length scale L in equation (2.5) would be the the length of the wall, while $T_w - T_0$ would be the temperature difference between the wall and the fluid. If e.g $T_w < T_0$, the fluid in vicinity of the wall would be cooled, its density increased, and it would therefore flow downwards along the wall. The thickness of both the momentum and the thermal boundary layer created by this temperature difference depends on fluid properties, and it can be expressed through the dimensionless Prandtl number:

$$Pr = \frac{\nu}{\alpha} \tag{2.6}$$

which is the ratio between momentum diffusivity and thermal diffusivity. For high Pr fluids ($Pr >> 1$), the inertia driven boundary layer is thicker than the buoyancy driven one, and vice versa for low Pr fluids($Pr << 1$). Turbulence is considered the most efficient way of mixing this "cold" fluid layer with the remaining fluid. A Grashof number criteria for transition to turbulent natural convection flow has been determined based on stability theory in equivalence with the high-Re criteria for forced convection.

A common way of categorizing natural convection flow is the product of these two parameter,namely the Rayleigh number:

$$Ra = Gr \times Pr = \frac{g\beta(T_w - T_0)L^3}{\nu\alpha} \tag{2.7}$$

Flow in subsea pipelines is usually characterized by high Rayleigh numbers, meaning that heat is efficiently mixed throughout the pipe due to natural convection. Loss of heat from the production fluid is governed by the heat flux boundary condition, $k(\partial T/\partial n) = q_w$, on the inner and outer pipe wall. In this equation, q_w is the wall heat flux, and n is the wall normal vector. Dimensional analysis reveal that this boundary condition can be described with a single dimensionless number called the Nusselt number(White [2006]). Equation (2.8) states that convection is the most efficient heat transfer mechanism.

$$Nu = \frac{q_w L}{k(T_w - T_0)} = \frac{q'}{q'_{pure-conduction}} \tag{2.8}$$

2.1.2 Scaling of experimental data

The objective of the current thesis was to study natural convection in a vertical dead-leg with a cold spot on top. Important questions raised here: what are the most important driving mechanisms for the flow, and how should the experimental data be scaled. The experiment consisted of two consecutive phases as depicted in figure 2.1, namely steady state and cool down.

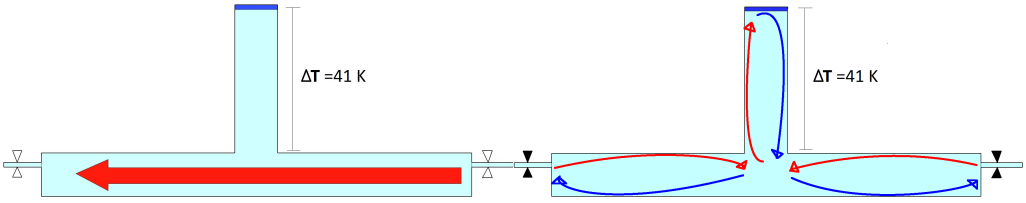

(a) Phase 1:Steady State (b) Phase 2:Cool down

Figure 2.1: The heat transfer mechanisms during the two phases of the experiment: (a) Steady state and (b) cool down

In phase 1, warm water was forced through the header at a constant flow rate, and was convected upward in the dead-leg in a manner of mixed convection(a combination of natural and forced convection). On top of the dead-leg, a cold spot set up a temperature differential of $41°C$, acting on a characteristic length scale of $D = 0.143$ m, triggering natural convection. During this phase, it was expected that heat would be efficiently mixed throughout the pipe in a combination of forced, mixed and natural convection.

During phase 2, natural convection would be the only important internal heat transfer mechanism. According to Bejan and Kimura [1980], it would occur as an end to end mechanism between the T-branch and the two opposite horizontal ends in the header. So when heat was extracted through the dead-leg wall and the cold spot, natural convection ensured effective heat exchange with the header.

Preliminary experiments indicated that the driving mechanism for internal natural convection in the current experiment would be the one created by the cold spot. A characteristic velocity scale was therefore chosen to be:

$$\sqrt{g\beta\Delta TL} \tag{2.9}$$

with β evaluated at 45 $°C$, $\Delta T = 41°C$ and $L = 0.143$ m.

2.2 Turbulence

During steady state circulation in the experiment, the flow was governed by $Re > 5000$ in the header, which is definitely in the turbulent regime. Large Rayleigh numbers and intrusive temperature sensors generated turbulent flow in the dead leg during both steady state and cool down. Turbulent flow is defined as "Irregular motion in which physical quantities (velocity,pressure,temperature) vary nearly randomly in time and space"(Reif [2014]). These variations also occur on a wide range of scales, which are all of importance. According to Kolmogorov (White [2006]), the smallest spatial scale is given by the viscosity of the fluid and the dissipation rate, while the largest(energy containing) scales depend on geometry. Separation of these scales are known to increase with the Reynolds number. This is also the case with the separation of temporal scales. The computational expense of simulating turbulent flow with all these scales resolved is proportional to $Re^{11/4}$.(Reif [2014]) (Note that the Reynolds number in this case is based on the root mean square of the velocity and not the bulk velocity.)

Even though non-linear equations can be solved numerically, the computational expense of a "real-life" simulation of turbulent flow goes far beyond what is technologically available today(Reif [2014]). In 1881 Osborne Reynolds(White [2006]) proposed the idea of decomposing the instantaneous quantities into a mean and a fluctuating component.

$$\begin{aligned}\tilde{u_i}(\mathbf{x},t) &= U_i(\mathbf{x},t) + u_i(\mathbf{x},t)\\ \tilde{p}(\mathbf{x},t) &= P(\mathbf{x},t) + p(\mathbf{x},t)\\ \tilde{T}(\mathbf{x},t) &= T(\mathbf{x},t) + t(\mathbf{x},t)\end{aligned}$$

The upper- and lower-case letters on the right hand side of the above equation describe the mean and fluctuating components respectively. In an engineering context, the mean quantities will yield important information. Ensemble averaging Eq. (2.1), (2.2) and (2.4) give rise to the Reynolds Averaged Navier-Stokes (RANS) equations and the Reynolds averaged continuity and heat equation. Written in index notation, these equations are given respectively as:

$$\frac{\partial U_i}{\partial t} + U_j\frac{\partial U_i}{\partial x_j} = -\frac{1}{\rho}\frac{\partial P}{\partial x_i} + \frac{\partial}{\partial x_j}(\nu\frac{\partial U_i}{\partial x_j}) + \beta g_i \Delta T - \frac{\partial}{\partial x_j}(\overline{u_i u_j}) \tag{2.10}$$

$$\frac{\partial U_i}{\partial x_i} = 0 \tag{2.11}$$

$$\frac{\partial T}{\partial t} + U_j \frac{\partial T}{\partial x_j} = \frac{\partial}{\partial x_j}(\alpha \frac{\partial T}{\partial x_j}) - \frac{\partial \overline{u_j t}}{\partial x_j} \tag{2.12}$$

Through averaging the convective terms in equation (2.1) and (2.4) two new terms have appeared. The term $-\frac{\partial}{\partial x_j}(\overline{u_i u_j})$ contains the Reynolds stresses, and is the ensemble averaged effect of turbulent advection on the mean flow field (Reif [2014]). The term $\overline{u_j t}$, is named the turbulent heat flux.

With the intention of reducing the computational expense of a "real-life" simulation by filtering out the fluctuating quantities in the flow, many new unknowns have been introduced. With the number of unknowns far exceeding the number of equation, finding new transport equations is crucial. By substituting equation (2.10) from equation (2.1), and doing a series of algebraic manipulations, one can obtain a transport equation for the Reynold stresses $\overline{u_i u_j}$. However, this equation involves additional unknowns, and the equation system is still unclosed.

2.2.1 Closure relations

A way of modelling the stress tensor was introduced by Boussinesq(White [2006]). If setting $i = j$ in the Reynolds stress equation and dividing by 2, the result is a much simpler scalar equation for the turbulent kinetic energy(TKE), $k = 0.5\overline{u_i u_i}$. The idea behind the linear eddy-viscosity hypothesis is to express the Reynold stresses as a function of TKE and mean shear

$$\rho\overline{u_i u_j} = \frac{2}{3}\rho k \delta_{ij} - 2\mu_T S_{ij} \tag{2.13}$$

,where $S_{ij} = \frac{1}{2}(\frac{\partial U_j}{\partial x_i} + \frac{\partial U_i}{\partial x_j})$, δ_{ij} is the Dirac delta, and μ_T is named the eddy viscosity. The most common way of modelling the eddy viscosity is to assume it is given by the TKE and the dissipation

$$\mu_T = C_\mu \rho \frac{k^2}{\epsilon} \tag{2.14}$$

,where C_μ is a constant that needs to be determined. In the widely used $k - \epsilon$ model, RANS equations and separate transport equations for k and ϵ are solved:

$$\rho\frac{\partial k}{\partial t}+\rho U_j\frac{\partial k}{\partial x_j}=\frac{\partial}{\partial x_j}[(\mu+\mu_T)\frac{\partial k}{\partial x_j}]+P_k-\rho\epsilon \tag{2.15}$$

$$\rho\frac{\partial \epsilon}{\partial t}+\rho U_j\frac{\partial \epsilon}{\partial x_j}=\frac{\partial}{\partial x_j}[(\mu+\frac{\mu_T}{\sigma_\epsilon})\frac{\partial \epsilon}{\partial x_j}]+\frac{C_{\epsilon1}P_k-C_{\epsilon2}\rho\epsilon}{k/\epsilon} \tag{2.16}$$

In equations (2.15) and (2.16), the production $P_k=-\rho\overline{u_iu_j}\frac{\partial U_i}{\partial x_j}$, and the dissipation $\epsilon=\nu\overline{\frac{\partial u_i}{\partial x_j}\frac{\partial u_i}{\partial x_j}}$. Through a series of assumptions and experiments, the constants $C_{\epsilon2}$,$C_{\epsilon1}$, σ_ϵ and C_μ have been determined. After ν_T (μ_T/ρ) has been calculated, the turbulent heat flux is calculated as $\overline{u_jt}=-\alpha_t\frac{\partial T}{\partial x_j}$. The term α_t is modelled based on scale analysis. A turbulent Prandtl number can be written as $Pr_t=\nu_t/\alpha_t$. Since both terms in this equation stem from the same mechanism of time averaging, their ratio should be of order unity(White [2006]). Experimental measurements indicate $Pr_t\approx0.9-1.0$.

Another way of closing the set of equations is to assume that the eddy viscosity can be described by the inverse of the turbulent time scale $\mu_T=(\rho k)/\omega$. Transport equations for ω can be obtained in the same manner as for ϵ and is given in Durbin and Reif [2011].

One can compare the two models through substituting the relation $\omega=\epsilon/(C_\mu k)$ into equation (2.16). This reveals that the $k-\epsilon$ model contain complex non-linear damping terms, which has been proven problematic in near wall modelling. On the other hand, the $k-\omega$ equation is said to be very sensitive to the conditions in the free stream (ANSYS [2013b]). Therefore a blending term is often used in simulations to enable a $k-\omega$ formulation close to the solid wall, and a $k-\epsilon$ formulation outside the boundary layer. Such models are named low-Re $k-\epsilon$ models.

2.2.2 Wall functions

Looking at equation (2.15) one can see that production of turbulence is given by the mean shear, which is largest close to the wall, stating that turbulence is generated close to the wall. The accuracy of the near wall modelling is crucial in order to obtain correct results in the rest of the domain. Even with the use of scalar equations to describe turbulence, the computational expense is still high due to strict requirements on near wall resolution. Instead of resolving the boundary layer, wall functions can be used as introduced by Theodore Von Karman(White [2006]). He stated that

in the inner and outer boundary layer, the velocity is given by the distance from the wall. However, the wall equations were derived by assuming high Reynolds numbers, and should therefore be avoided in areas where natural convection is the main flow mechanism. The low-Re $k-\epsilon$ models are able to resolve the boundary layer if the numerical grid is fine enough. In chapter 4, the numerical grid used in this thesis will be presented.

Chapter 3

Experimental set-up and Measuring Techniques

3.1 Experimental set-up and Materials

In this section the details regarding the experimental set-up and techniques are presented, along with material properties and case descriptions. The experimental set-up was a production pipeline made in 5 mm thick plexiglass with inner diameter of 143 mm, with water as production fluid. It was situated on top of a wooden table, but with an insulating Styrofoam board between to prevent heat exchange with it. The pipeline consisted of a 3 m long horizontal header connected to a vertical dead-leg of 1 m, forming a T-pipe. The header was insulated with 19 mm thick Armaflex, while the dead-leg was kept uninsulated and carried a cold spot on top. The cold spot was a circular aluminium plate used as a lid on the dead-leg. It was cooled by circulating water through channels in its interior, and its bottom surface (Ø 143 mm) was in contact with the water on top of the dead-leg. Water temperature was measured with 6 intrusive PT 100 sensors, while type k and type t thermocouples reported temperatures on the header and dead-leg plexiglass wall respectively. To improve accuracy, 3 thermocouples were used at every measurement point. Experimental set-up is sketched in figure 3.1, and the sensor positions with respect to the sketched coordinate system are given in table 3.1. As illustrated, the y- and z-axis are aligned with the vertical and horizontal direction respectively, while the x-axis points out of the figure.

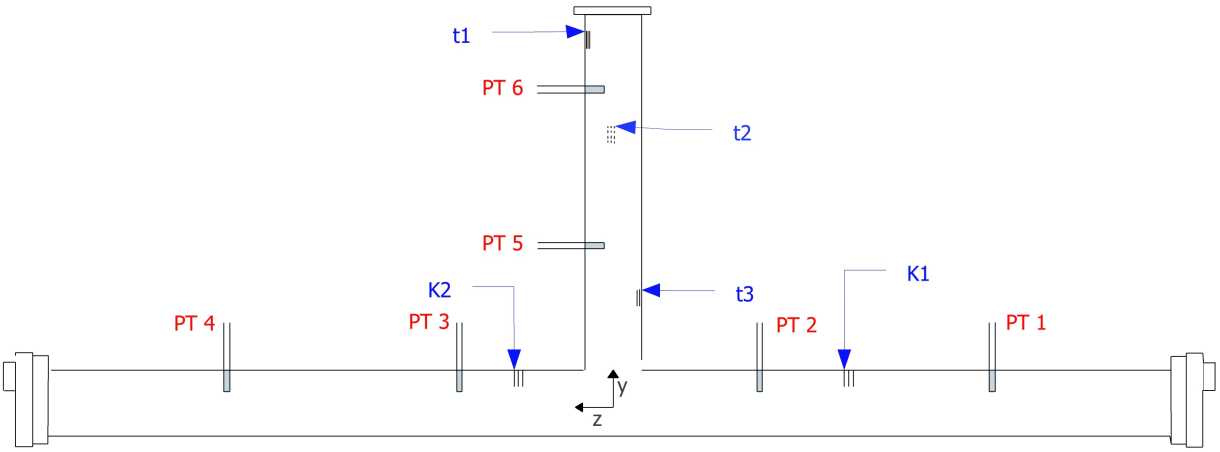

Figure 3.1: T-pipe geometry and sensor positions

Table 3.1: Position of internal PT sensors, and external thermocouples of type k and t.

Sensor-name	**Sensor position** X[m]	Y[m]	Z[m]	**Sensor-name**	**Sensor position** X[m]	Y [m]	Z[m]
PT1	0	0.0225	-0.977	t1	0	0.95	0.0765
PT2	0	0.0225	-0.377	t2	-0.0765	0.797	0
PT3	0	0.0225	0.396	t3	0	0.25	-0.0765
PT4	0	0.0225	0.996	k1	-0.05	0.0578	-0.677
PT5	0	0.397	0.023	k2	-0.05	0.0578	0.233
PT6	0	0.797	0.023				

The materials used in the experiment are listed in table 3.2, along with their thermal properties. The cold spot was made in aluminium, and was sealed with a plexiglass lid on top. A sketch of the cold spot geometry is given in appendix A. Armaflex was attached to the header using duct tape with similar thermal properties. Water and air properties evaluated at 45 degrees are listed in table 3.3.

Table 3.2: Properties for experimental materials

Material	**Material properties**		
	Density [kg/m^3]	Heat capacity [J/Kg K]	Thermal conductivity [J/m K]
Armaflex	50	1200	0.036
Plexiglas	1100	1470	0.2
Stainless steel	7850	450	14.2
Aluminum	2702	903	237
Hose	1500	2500	1

Table 3.3: Properties of water and air evaluated at 45°C

Fluid properties		Water	Air	Units
Density	ρ	989.8	1.1098	kg/m^3
Heat capacity	C_p	4066.5	1007.2	$J/(kg \cdot K)$
Dynamic viscosity	μ	0.000579	0.00001938	$kg/(m \cdot s)$
Thermal conductivity	k	0.6384	0.02744	$W/(m \cdot K)$
Coefficient of thermal expansion	β	0.000314	0.00314	$1/K$

3.2 Instrumentation and measurement techniques

3.2.1 Temperature sensors

To measure the wall temperature, type k and t thermocouples were attached to the plexiglas wall using ACRIFIX 116 glue. A type k thermocouple consists of chromel and alumel. When these metals are exposed to a temperature gradient, as in ΔT between pipe wall and ambient, they will both generate their unique voltage. It is the difference between these voltages that is measured, and it varies almost linearly with temperature. The PT 100 sensors measure the resistance of a platinum element, a resistance that varies with temperature. Its resistance at 0 degrees is 100 ohms, and it varies almost linearly with temperature(Omega [1987]).

The offset for each sensor was found through measuring the room temperature, and subtracting the mean room temperature based on the average of

all PT elements, whose accuracy exceeds the thermocouples. To compensate for a lower accuracy of thermocouples, three sensors were used at every wall measurement point, and results presented in this thesis are averages of these.

3.2.2 Particle Image Velocimetry (PIV)

PIV is a way of translating a physical observation of a velocity field into numerical values. The goal was to estimate the water velocities in the dead-leg. Water was seeded with naturally buoyant polyamide particles of $50\mu m$ diameter, that gets illuminated by a light source. A double pulsed laser created a light sheet in the dead-leg, illuminating the particles. It triggered a high resolution camera to take a picture at each of the two pulses separated by a known Δt. In Fig. 3.2, an image pair taken during steady state circulation with $\Delta T = 15$ ms is depicted.

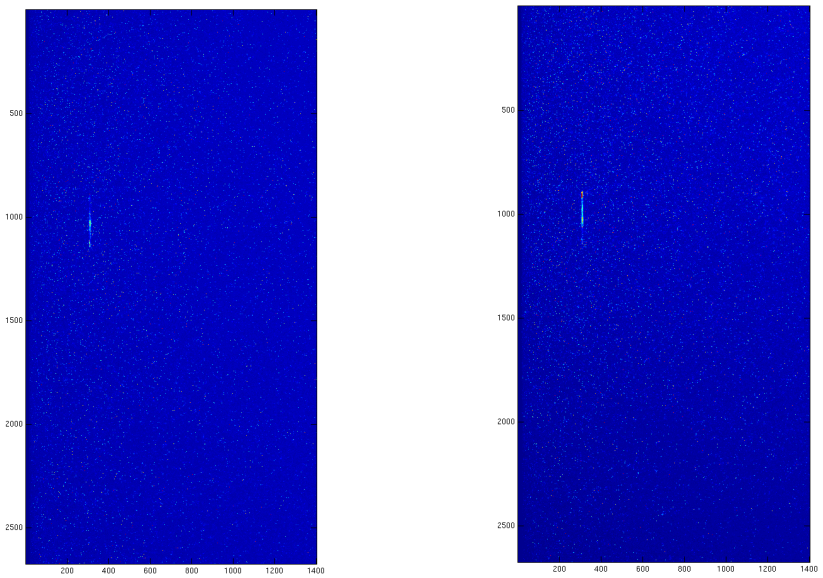

(a) Image A

(b) Image B

Figure 3.2: PIV: Two pictures separated by $\Delta T = 15ms$ taken of the dead-leg during steady state

When looking at the two photos, it is not easy to track the movement of individual particles seen as each photo consists of 2670x1400 pixels. However, if dividing both pictures into e.g 64x64 pixel sub windows, particle tracking within each sub window can be achieved with pen and paper even though it would be a tedious process. Letting a computer do this work would defi-

nitely be time saving, but the computer would have to be told what to look for, and how to look. Where we observe particles, the computer see pixels of varying light intensity, with peak values at particle locations. Cross correlation is a pattern matching technique that can be used for measuring similarity between two pictures. The pictures may be divided into MxN sub windows, and the pixel values in these sub windows may be given by the functions f(i,j) and g(i,j).

$$R(m,n) = \frac{1}{N^2} \frac{\sum_{M,N} f(i,j)g(i+m,j+n)}{|\sum_{M,N} f(i,j)^2 \sum_{M,N} g(i+m,j+n)^2|^{1/2}} \tag{3.1}$$

If these functions are multiplied with each other in different overlapping positions, it will result in intensity values which can be plotted on a cross correlation plane. The overlapping position resulting in the highest peak in this plane, gives the pixel displacement of the particles in the sub window. By repeating this calculation for all the sub windows, one obtains the pixel displacement of all visible particles/patterns in the picture. By dividing with Δt one gets a velocity field in pixel/second.

To get velocities in m/s, a relationship between pixels and world coordinates was obtained by taking a picture of a physical coordinate system lowered into the dead-leg(see Fig. 3.3). The world coordinates were known at all points on the coordinate system, and it was therefore possible to express pixel distance in meters. The known Δy between the marked points in figure 3.3 is 5 mm, and there is a total of 80 pixels between them. Therefore, 1 pixel $= 6.25e^{-5}$m in this part of the photo. With enough coordinates given, one gets a relationship between pixel and world coordinate for the entire picture, regardless of pipe curvature. This procedure was carried out after every experiment.

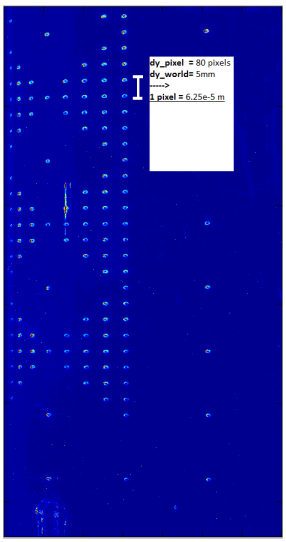

Figure 3.3: Coordinate system

By cross correlating an image pair, one obtains an instantaneous velocity field. As introduced in chapter 2, the instantaneous velocity can be divided into a mean and a fluctuating component. Ensemble averaging over N samples is a way of filtering out the fluctuating component. However, this requires the fluctuations to be scattered around a well defined mean. Kolaas et al. [2014] showed that convergence towards a mean can be ensured by minimizing the variance within consecutive sub windows through acquiring enough samples. The turbulent quantities can then be evaluated by subtracting the mean velocity from the instantaneous velocity in each sub window.

In the current experiment, a set of 31 image pairs with a resolution of 2670x1400 pixels were acquired over a period of 186 seconds. Improved temporal resolution for consecutive image pairs was not possible due to data transfer limitations. Post-processing of image pairs was done in Digiflow, using an interrogation window size of 64x64 pixels with 75% overlap.

3.2.3 Experimental uncertainties

There were many uncertainties in this experiment. First of all, there were systematic errors for the components involved in the experiment(see figure 3.4). These errors were believed to be systematic, in the sense that they remained constant for all experiments.

1) Cooler : $\pm 0.01°C$
2) Pump : $\pm 0.5\%$ $[kg/h]$
3) Thermocouple type k: $\pm 2.2°C$
4) Thermocouple type t: $\pm 1.0°C$

Systematic errors could also have been induced by the MGC plus, the laser delay box, and through thermally altering the thermocouples by attaching them with ACRIFIX 116 glue. Second, by executing the experiment manually, random errors were introduced:

1) Cool down initiation
2) High resolution camera triggering
3) Coordinate system bias

To initiate the cool down, the pump was stopped, two valves were closed, a stop watch was set, and the heat exchanger was turned off . During cool down the camera was triggered at every 5 minutes interval for 3 hours, and at the end of the experiment, a coordinate system was lowered into the

dead-leg. Since all these steps were conducted manually, minor deviations between experiments were unavoidable. To what degree these random errors influenced the repeatability of the experiment is assessed in Chapter 5.

Ayati et al. [2014] highlighted the main sources of noise that influence the accuracy of a PIV measurement. Considered important to this thesis were the ones affecting the first order statistics, i.e mean velocity. First of all, the maximum in-plane displacement of a particle was assessed. If it exceeded the interrogation window(IW) size, the image pair would become uncorrelated, and the resulting displacement vector would be due to background noise. In this thesis an IW size of 64x64 pixels was found to be sufficient. Second, the out-of-plane motion was assessed, and it was concluded that it was of order $0.02l_z$, with l_z begin the laser sheet thickness of $5mm$. This was based on a maximum velocity of $0.36m/s$ at $Re = 45,000$, with $\Delta t = 100\mu s$. Compared to the experiment in this thesis, the maximum vertical velocity was found to be $0.03m/s$. Since the out-of-plane velocity was not believed to exceed this, it would be less than $0.09l_z$(when $\Delta t = 15ms$), and therefore not considered problematic. Third, the influence of optical distortion and reflection at the pipe wall was considered. In the present study, there was reflection on the dead-leg wall, which lowered the near wall resolution and increased the noise level. Fourth, the errors linked to size and passivity of the tracer particles were discussed, and found negligible when the Stokes number $St << 1$. In this thesis, polyamide particles with a diameter of $d_p = 50\mu m$ and a density of $\rho_p = 1050kg/m^3$ were used. These particles were considered passive in a previous study by Grafsrønningen [2012] for natural convection flow around heated cylinders, based on estimates for the Stokes number. Following the same train of thoughts, the particle settling time was first calculated: $\tau_T = (\rho_p d_p^2)/(18\mu)$. With water properties evaluated at $45°C$, the settling time was $0.00025s$. The Stokes number was calculated to be $\tau_T/T_0 = 0.00023$, with $T_0 = D/U_0$, and U_0 is given in Eq. (2.9). This confirmed the passivity of the particles in terms of mean flow characteristics, which were the main focus in this study. Finally, errors due to peak-locking was discussed. Peak-locking is a bias towards integer pixel values when calculating the pixel displacement vector. Through using the commercial code Digiflow, the author argued that this bias was minimized. Post-processing of image pairs in this thesis was also conducted in Digiflow, and therefore not believed to be biased. In depth discussion on peak-locking is given in Sveen and Cowen [2004].

3.3 Experiment summary and case description

The main components involved in the experiment are sketched in figure 3.4. Before initiating the experiment, water was heated to 70°C to remove air voids which could potentially attach to the inner pipe wall and sensors during the experiment. After the experiment was initiated, the remaining air in the system was removed by elevating the wooden table, and opening the top valve. Water was pumped into the header at a constant flow rate measured

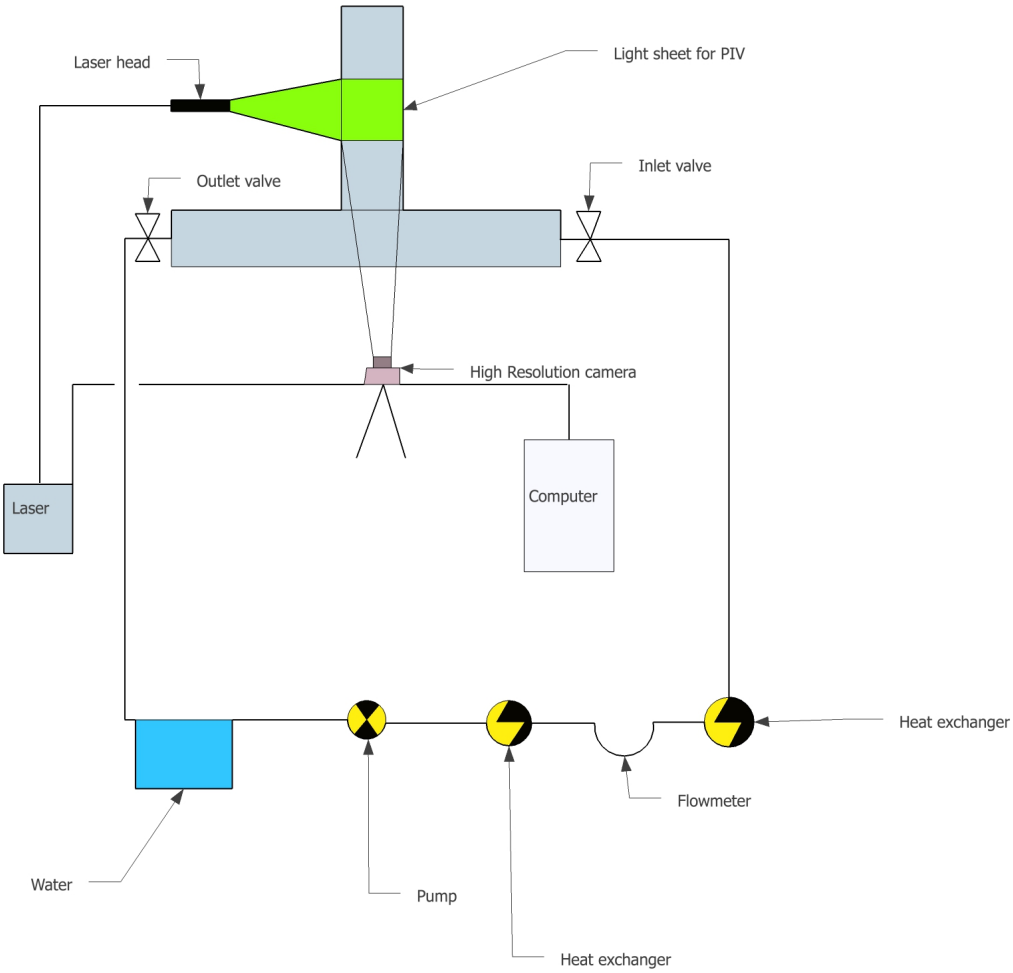

Figure 3.4: Experimental components

by a flow meter, and a constant temperature controlled by heat exchangers with PID controllers. Temperatures were measured with 6 intrusive PT100 sensors, and 5x3 pipe-wall mounted thermocouples of type k and t. With

the use of a high resolution PCO 4000 camera and an ICE^{450} laser, PIV was used to gain two dimensional velocity data in the dead-leg. After gathering temperature and velocity data for 2 hours with steady state circulation, cool down was initiated by turning off the pump, and closing the inlet and outlet valves. During a 3 hour cool down, velocities were measured every 5 minutes, and temperatures were logged continuously.

The high resolution camera used in the experiment took image pairs with good temporal resolution, but was restricted due to data transfer capacity. At every 5 minute interval during cool down, it was therefore possible to obtain no more than 31 image pairs. Due to the flow being turbulent, it was decided to use data from several consecutive runs in order to improve the quality. However, this gave requirements on repeatability, which is scrutinized in chapter 5.

Some important parameters in this experiment were varied in order to look at sensitivity. In Parameter study 1(P1) the downstream side of the wooden table was elevated to an angle of 2.4°. Both velocities and temperatures were measured. As a result of analysing experimental data, another parameter study seemed necessary. In Parameter study 2(P2), water was added during cool down to prevent volume reduction due to increased density. This was done for both horizontal and inclined experimental set-up. Only temperatures were measured in this study, and one repetition was therefore sufficient.

Experiment	Description	Repetitions	Measurements
Main experiment	Horizontal	4	Velocity,Temperature
P1: 2.4°	Inclined	3	Velocity,Temperature
P2: Water addition	Horizontal, Inclined	1	Temperature

Chapter 4

Numerical model

4.1 Geometry

A preliminary CAD model was supplied by FMC Technologies, representing the experimental set-up without insulation and cold spot. In order to customize the model to this study, the following modifications were made in ANSYS Geometry: **(1)**Addition of 19mm thick insulation, **(2)**Deadleg plexiglass endplate replaced with a 2 mm thick aluminium plate, **(3)**Removal of PT100 sensor on top of dead leg, **(4)**Top valve rotated 180 degrees.

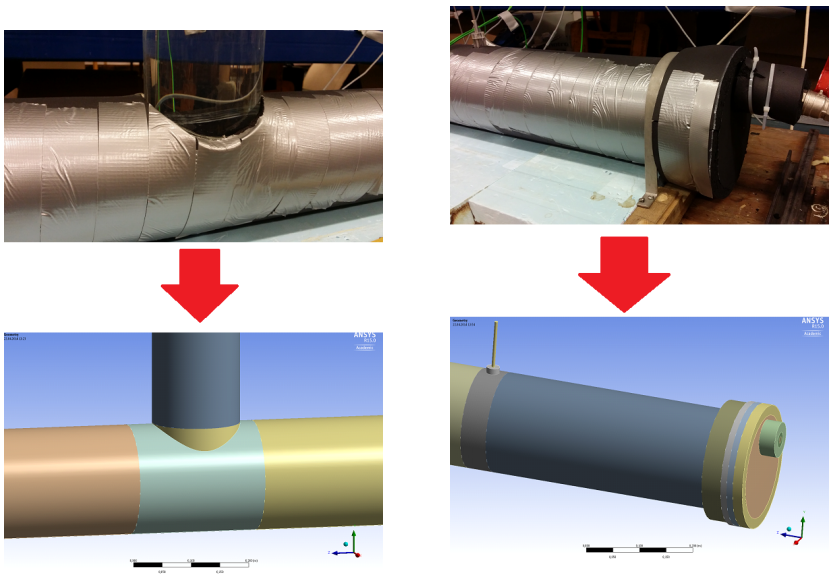

(a) T-branch (b) Inlet

Figure 4.1: Geometry with 19 mm insulation: Experimental vs. CAD

Figure 4.1 gives a comparison of the experimental and numerical insulation for the T-branch and the inlet, clearly stressing the need of a simple experimental geometry. The duct tape seen in this figure was found to have similar thermal properties as that of Armaflex, and the error due to not including this in the model was expected to be negligible.

4.2 Meshing

Meshing was conducted using ANSYS Meshing, in Workbench version 15.0. ANSYS meshing is a software that simplifies the meshing process compared to other software such as ICEM CFD, but is less robust. Considering the simplicity of the experimental geometry , ANSYS meshing was found adequate. A coarse mesh with decent quality will be created automatically if no constraints are defined. To get a mesh suited for this particular study, mesh controllers were inserted as recommended by Grafsrønningen and Jensen [2014].

Table 4.1: Important mesh parameters

	Mesh
Number of nodes	1.53e6
Radial cell count insulation	6
Radial cell count unisolated piping	8
Radial cell count insulated piping	5
Cirumferential cell count on piping	60
First layer height piping	2e-4 [m]
Numbers of layers piping	12
Body sizing on piping	4e-3 [m]
Body sizing on insulation	4e-3
Body sizing on fluid	7e-3 [m]

Hexahedral sweep mesh needs to be generated before tetrahedral mesh on adjacent parts, and since not all parts were sweepable, meshing was executed in the following order:

1 Sensors+brackets (hexahedral sweep + edge sizing)

2 Piping 1 + insulation 1(Hexahedral sweep + edge sizing)

3 End plates (tetrahedral body sizing)

4 Piping 2 (hexahedral thin-sweep)

5 Piping 3 (tetrahedral body sizing)

6 Insulation 2(tetrahedral body sizing)

7 Fluid near pipe wall (hexahedral inflation layer)

8 Fluid (tetrahedral body sizing)

Hexahedral elements were demanded on the sweepable solid parts of the geometry, simply due to the radial symmetry of the heat transfer mechanism. Demanding edge sizing and mapped face meshing on each side of sweepable bodies reduced the risk of mesh dependent solutions, and enabled the circumferential cell count to be set. In figure 4.2, the mesh resulting from the constraints listed in table 4.1 can be seen. The hexahedral sweep mesh with edge sizing was used on sensors, and on sweepable insulation and pipe wall parts. The remaining non sweepable solid parts were meshed using either thin-sweep, or body sizing. Body sizing was also applied to fluid parts, but with inflation layers close to the pipe wall.

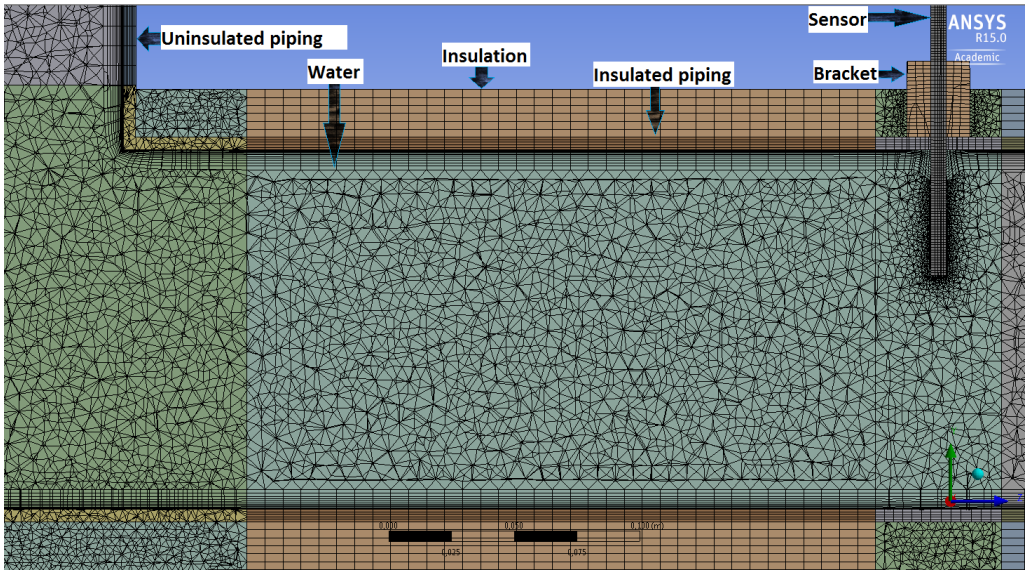

Figure 4.2: Show result of different size constraints and names of body parts. Water was meshed according to step 7 with 8 close to the wall, insulated piping with 2/4/5, and insulation with 2/6.

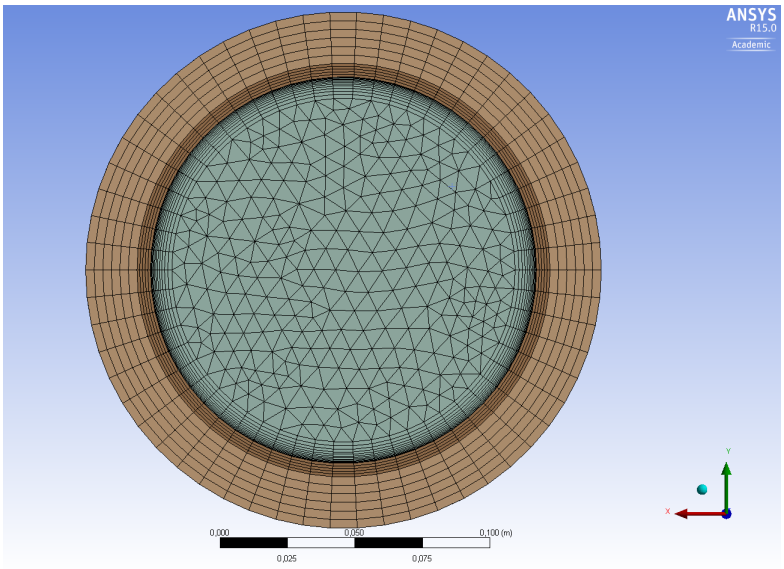

Figure 4.3: Circumferential symmetry in meshing of pipe, insulation and fluid (meshing 2,7,8)

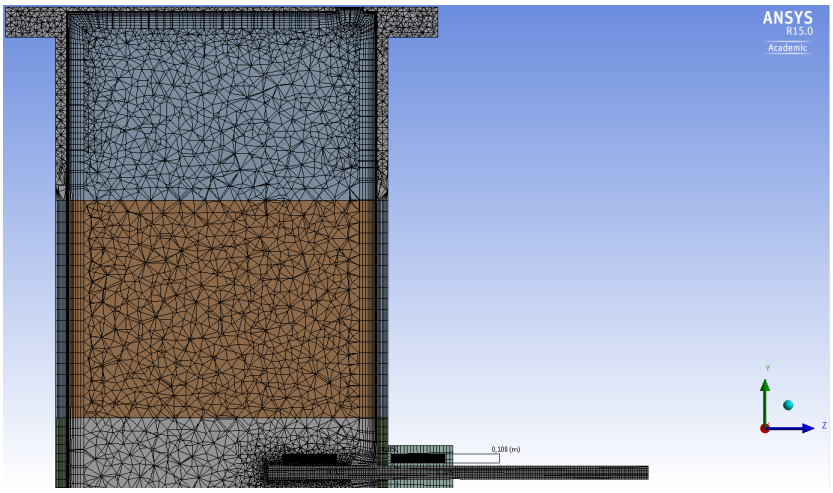

Figure 4.4: Meshing near cold spot

4.3 Case definition

Simulations were set up in ANSYS CFX pre, mimicking the experimental conditions. The model only included the pipe itself, and not the surrounding air, and it was necessary to specify boundary conditions on all external surfaces. All material properties along with fluid PVT tables and external heat transfer equations were given as input data.

4.3.1 Boundary conditions

4.3.1.1 Convection heat transfer

The main external heat transfer was expected to be due to convection and radiation. According to Churchill and Chu [1975] the external Nusselt number on both horizontal and vertical pipe walls can be expressed as:

$$\overline{Nu} = \left[A + \frac{BRa^{1/6}}{\left(1 + (C/Pr)^{9/16}\right)^{8/27}} \right]^2 \tag{4.1}$$

where the constants A,B and C are given in table 4.2. Rayleigh numbers were calculated using equation (2.7) with the length scale being the diameter and the length of the pipe for the header and the dead leg respectively.

Table 4.2: Constants used in calculating the Nusselt number on both horizontal and vertical cylinder walls

Constants	**Header**	**Dead leg**
A	0.6	0.825
B	0.387	0.387
C	0.559	0.492

4.3.1.2 Radiation heat transfer

It was also necessary to model the radiation from the external surfaces. According to black body radiation theory, external heat loss due to radiation is given by:

$$q_{rad} = \epsilon\sigma(T_w - T_a)^4 \tag{4.2}$$

where ϵ is the emissivity of the wall material, σ is the Stefan Boltzmann constant, T_w is the wall temperature and T_a is the ambient temperature. The emissivity of plexiglass and armaflex were 0.86 and 0.84 respectively.

4.3.1.3 Adiabatic- no heat transfer

As mentioned introductory, the pipe was situated on top of Styrofoam, minimizing the heat exchange from the circumferential surface area in contact with it. The bottom surface was therefore treated as an adiabatic wall. Heat exchange through closed valves was also treated as adiabatic.

4.3.1.4 Cold spot

As shown in figure 4.5, the numerical cold spot does not share the same complex geometry as the experimental one. It was modelled as a flat plate with a valve in the numerical model. Experiments proved that the addition

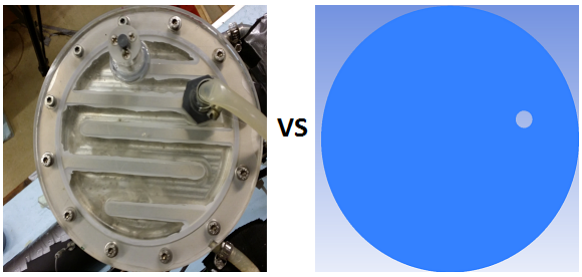

Figure 4.5: Experimental vs Numerical cold spot geometry

of a cold spot on top of the dead-leg had a major impact on both flow character and cool down times. Extra consideration was therefore directed towards modelling this external boundary condition as realistic as possible.

Cold spot 1: Constant temperature
Assuming that the circulating water created a constant wall temperature in the experiment, an isothermal temperature of $4°C$ was set uniformly on the numerical aluminium plate.

Cold spot 2: External Heat Transfer Coefficient
An external heat transfer coefficient was set on top of the aluminium plate. The EHTC was found with a correlation based on turbulent duct flow:

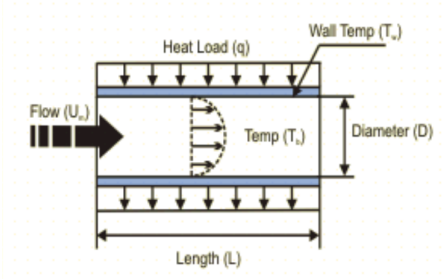

Figure 4.6: EHTC based on turbulent duct flow

$$Re = \frac{\rho u_m D}{\mu} \tag{4.3}$$

$$f = \left(0.79 \log\left(Re\right) - 1.64\right)^{-2} \tag{4.4}$$

$$Nu = \frac{\left(\frac{f}{8}\right)\left(Re - 1000\right)Pr}{1 + 12.7\left(\frac{f}{8}\right)^{0.5}\left(\left(Pr\right)^{2/3} - 1\right)} \tag{4.5}$$

$$h = \frac{Nuk}{D} \tag{4.6}$$

where u_m in the channel was based on the flow rate of the cooler pump, $\dot{m} = 5.18e^{-2}kg/s$, and D was the height of the channel. The result was an EHTC coefficient of $h = 589[W/(m^2K)]$. However, the geometry of the channel was not included in the model, only a $2mm$ thick aluminium plate with $D = 20cm$(see figure 4.5). Since it was required to set an overall EHTC on the entire surface, the calculated h was scaled with the ratio of surface area in contact with water.

$$h_{eff} = h\left(\frac{A_{water}}{A_{lid}}\right) = 589 \cdot 0.4748 \approx 280 \tag{4.7}$$

The boundary condition on top of the aluminium plate was set to $h = 280$ $W/(m^2K)$, with an outside temperature of 4°C.

Cold spot 3: Heat flux
The third boundary condition in the numerical model was based on more data from experiments. The gradient across the lid was found to be $\Delta T_{lid} = (T_{out} - T_{in}) = 1.53°C$ during steady state. Inlet temperature was set by the cooler, while the outlet temperature was measured using a PT sensor. During this phase the heat loss per unit time was found to be $\dot{Q} = \dot{m}C_p\Delta T = 5.18e^{-2}kg/s \cdot 4200J/(KgK) \cdot 1.53K = 376W$. Dividing this effect with the area of the aluminium lid as defined in the numerical model, the heat flux through the boundary surface was obtained. When the pump was shut off, the cooling effect decreased with time. Heat loss data was therefore logged continuously during the 3 hour cool down experiment, and inserted as a transient boundary condition in CFX.

4.3.1.5 Summary of boundary conditions

Boundary conditions used for all simulations are sketched in figure 4.7. The inlet and outlet condition is different for the two phases Steady State(A) and Cool down(B). The three different approaches to modelling the boundary condition on the cold spot(I,II,III) is further summarized in table 4.3

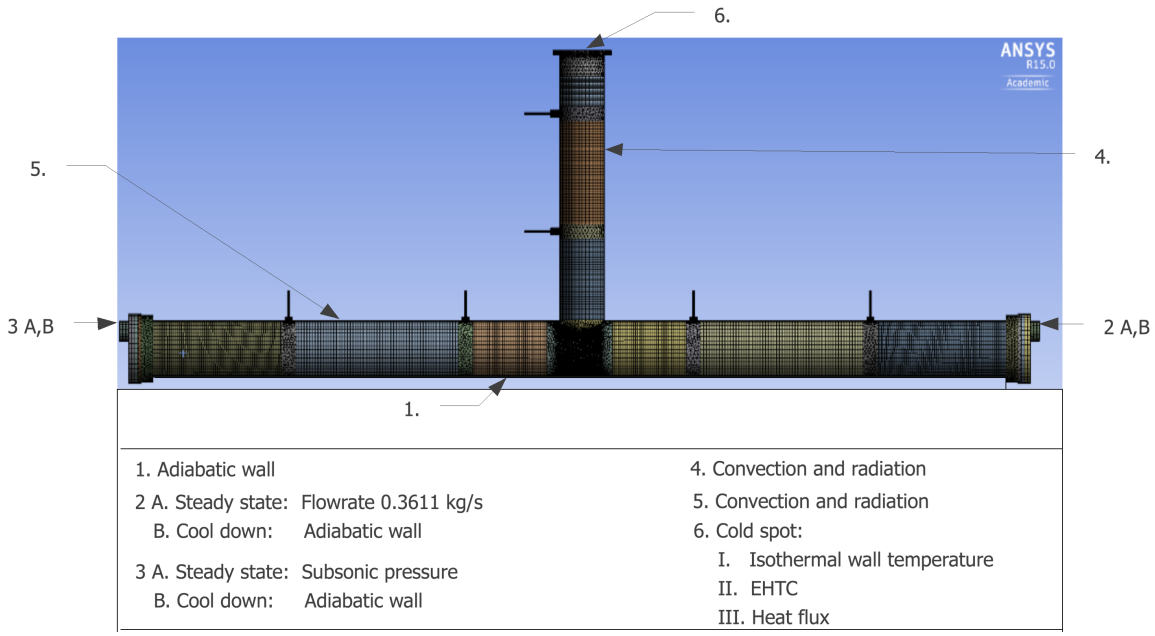

Figure 4.7: Numerical boundary conditions

Table 4.3: Boundary conditions used to model the cold spot

Parameter study	Boundary Condition		Outside Temperature
Cold spot 1	Temperature	4 $°C$	N/A
Cold spot 2	EHTC	238 $W/(m^2K)$	4 $°C$
Cold spot 3	Heat flux	q(t) $W/(m^2)$	N/A

4.3.2 Initial conditions

Initially, the velocities throughout the domain were zero and temperatures were set to $T_0 = T_{inlet}$ for fluid regions and all solid parts, with the exception of the cold spot, where $T_0 = 4°$C. Turbulence intensity were set to 5% with $\frac{\mu_t}{\mu} = 10$ as recommended when lacking information about the inlet turbulence(ANSYS [2013a]).

4.4 Simulation

In this section the details regarding solver equations,numerical schemes, simulation controls and convergence criteria are presented.

4.4.1 Turbulence model

A k-ω SST turbulence model was used as recommended by Grafsrønningen and Jensen [2014], and the main idea behind a k-ω based turbulence model was described in chapter 2. The SST formulation of the k-ω model, including buoyancy effects, is expressed in CFX as(ANSYS [2013b]):

$$\frac{\partial}{\partial t}(\rho k) + \frac{\partial}{\partial x_j}(\rho U_j k) = \frac{\partial}{\partial x_j}[(\mu + \frac{\mu_t}{\sigma_{k3}})\frac{\partial k}{\partial x_j}] + P_k - \beta'\rho k\omega + P_{kb} \tag{4.8}$$

$$\begin{aligned}\frac{\partial}{\partial t}(\rho\omega) + \frac{\partial}{\partial x_j}(\rho U_j \omega) = \frac{\partial}{\partial x_j}[(\mu + \frac{\mu_t}{\sigma_{\omega 3}})\frac{\partial \omega}{\partial x_j}] + \alpha_3\frac{\omega}{k}P_k - \beta_3\rho\omega^2 \\ + P_{\omega b} + (1-F_1)2\rho\frac{1}{\sigma_{\omega 2}\omega}\frac{\partial k}{\partial x_j}\frac{\partial \omega}{\partial x_j}\end{aligned} \tag{4.9}$$

where the terms $P_{\omega b}$ and P_{kb} are production of ω and k due to buoyancy:

$$P_{kb} = \frac{\mu_t}{\rho\sigma_\rho}\rho\beta g_i\frac{\partial}{\partial x_i}T \tag{4.10}$$

$$P_{\omega b} = \frac{\omega}{k}((\alpha+1)C_3 max(P_{kb},0) - P_{kb}) \tag{4.11}$$

The constants in equation (4.8) and (4.9) are given in ANSYS [2013b]. The advantage of $k-\omega$ SST is that it is actually a combination of the $k-\epsilon$ and $k-\omega$ model. As mentioned previously, $k-\omega$ makes it possible to resolve the flow all the way down to the viscous sub layer, while the $k-\epsilon$ model is less sensitive to inlet free-stream turbulence properties. The term F_1 is therefore equal to 1 close to the wall, and decreases to zero outside the boundary layer.

4.4.2 Steady state simulation

A physical time scale was set to 0.1 s and 1 s for the fluid and the solid region respectively, and the convergence RMS criteria for all variables was $1e^{-6}$. Given the transient behaviour of the flow, the stability of the steady state solution was tested by running a transient simulation with the output from the steady state simulation as initial condition, without changing the boundary conditions.

4.4.3 Transient scheme

The results from the steady state simulation were used as input data for the cool down simulation. A Second Order Backward Euler scheme ensured stability regardless of Courant number, but for accuracy, a maximum rms Courant number was set for the adaptive time stepping. Three coefficient loops were used. To capture the abrupt changes in flow physics as cool down was initiated, an initial time step was set to $\Delta t = 1e^{-6}s$. As the simulation progressed, the time scale was augmented by increasing the maximum rms Courant number.

Chapter 5

Results

In this section, major experimental observations are described, along with a comparison between numerical and experimental results. All temperature data are reported at the sensor positions given in table 3.1. The location of PIV measurements, and the resulting velocity data is sketched in figure 5.1. An arrow points to where instantaneous velocities are plotted in the vicinity of the wall, $y = 0.5m$ and $z = 0.0705m$. Velocity profiles are plotted within the shown field of view, at $y = 0.5m$.

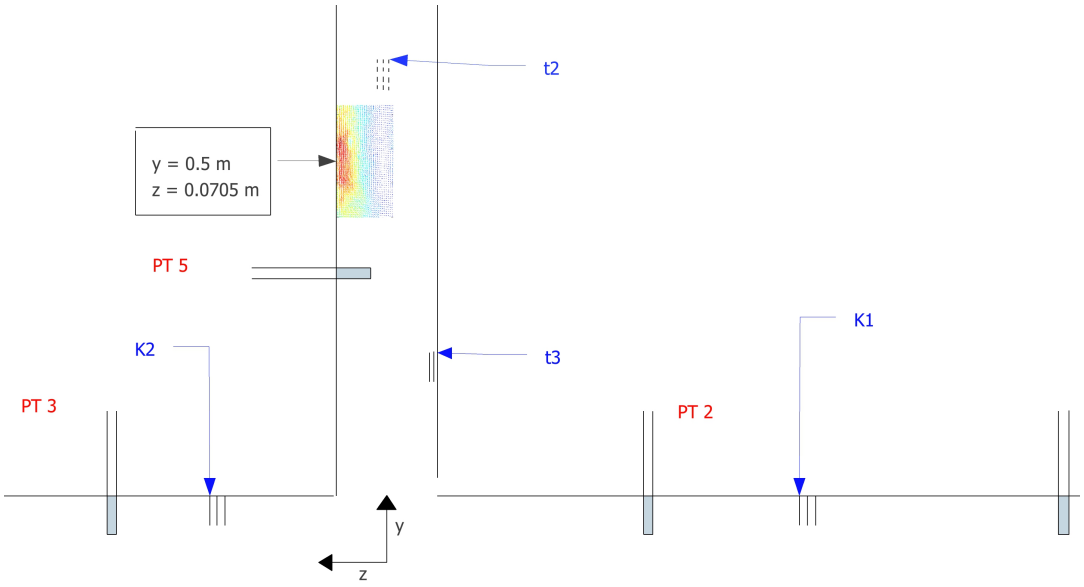

Figure 5.1: Sketch of measurement positions where experimental and numerical data are compared. Internal temperatures are reported at the PT sensors, wall temperature at the k and t sensors, and a black arrow points towards the field of view for velocity data.

5.1 Experimental analysis

The previous study by Grafsrønningen and Jensen [2014] reported agreement in experimental and numerical results with $k-\omega$ SST, using the same mesh sizing as presented in the previous chapter. Repeatability of the experiment was found adequate for both temperature and velocity data. A question raised in this thesis was whether the addition of a cold spot on top of the dead-leg would change these findings. Three runs were conducted without a cold spot for comparison. As depicted in figure 5.2, the effect of adding a cold spot on top of the dead-leg was very significant even in the header, where the final temperature after 3 hours of cool down was decreased by 4.5°C.

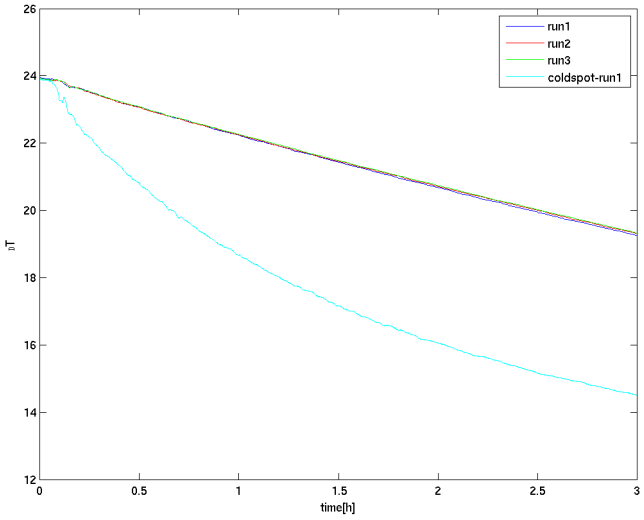

Figure 5.2: Difference in experimental temperature data with and without the cold spot for the PT1 sensor in the header

The depicted non-linear cool down behaviour was further investigated by looking at temperature data in the dead-leg where most of the heat was lost. Figure 5.3 illustrate temperature fluctuations of $\pm 0.3°C$ on top of the dead-leg(PT6 sensor), slowly diminishing during cool down. Considering how the average period of these fluctuations was approximately 30 seconds, they were not turbulent. During steady state, the cold spot only affected temperatures in the dead-leg. From figures 5.2 and 5.3 at $t = 0$, temperatures can be seen to be the same in the header, and lower by $3°C$ on top of the dead-leg.

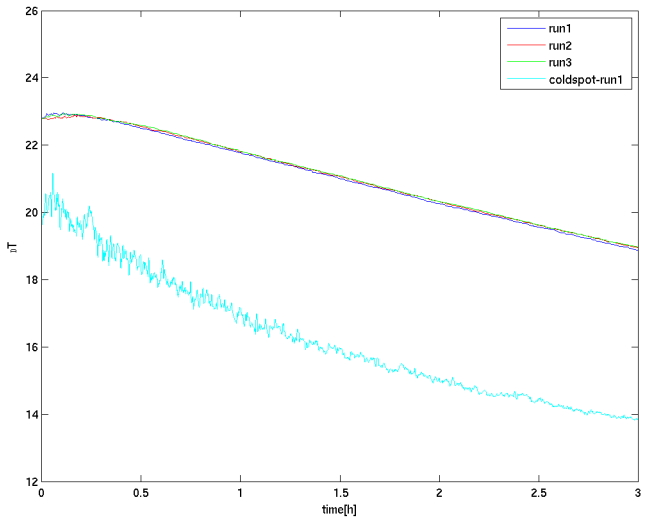

Figure 5.3: Difference in experimental temperature data with and without the cold spot for the PT6 sensor in the dead-leg

It was at this stage believed to be a correlation between the reduction in cooling rate and the diminishing of temperature fluctuations occurring after 40 minutes in Fig. 5.2-5.3. In parameter study 2, this correlation was found to be an insulating vacuum layer on top of the dead-leg caused by volume reduction. This layer prevented heat exchange due to convection between water and the cold spot, after about 40 minutes. In other words, the temperature fluctuations were caused by convection heat transfer. By removing the vacuum layer, temperature fluctuations in the dead-leg prevailed for 3 hours of cool down. The cooling effect obtained by adding a cold spot to the experiment was therefore increased, yielding a final temperature difference in the header of 9°C.

To get a better understanding of the kinematics governing the convective heat transfer mechanism, velocity data in the dead-leg from steady state experiments was analysed. In the previous study by Grafsrønningen and Jensen [2014], the mean velocity field during steady state was found by averaging over N uncorrelated samples, and compared with a numerical mean (RANS) velocity. However, with the addition of a cold spot, this approach resulted in the mean velocity being close to zero, and physical observations clearly contradicted this. As stated in chapter 3, it is possible to check convergence towards a "true" mean by looking at the decrease in variance with increasing number of samples. In this experiment, it was found that increasing the amount of samples did not reduce the variance. The periodicity observed in the temperature data was therefore believed to also be a trend in the velocity data. A criteria for filtering out the trend based on the average velocity in vicinity of the wall was made:

$$\tilde{u}_i(\mathbf{x},t) = \begin{cases} \tilde{u}_i^+(\mathbf{x},t) & \text{if nanmean}(\tilde{u_2}(1,:,t),2) > 0 \\ \tilde{u}_i^-(\mathbf{x},t) & \text{if nanmean}(\tilde{u}_2(1,:,t),2) < 0 \end{cases}$$

where $\tilde{u}_i(\mathbf{x},t)$ is the two dimensional instantaneous velocity field gained from PIV, and nanmean refers to an in-built MATLAB function that was set to calculate the average vertical velocity in the first column of sub-windows away from the dead-leg wall. After sorting all the instantaneous velocity fields into two categories, two mean velocity fields were found by averaging over all samples within each category separately. These two flow fields, depicted in Fig. 5.4, are dominated by a large scale convection cell, which is rotating clockwise(CW)(a) and counter-clockwise(CCW)(b). The magnitude of the convection cell velocity ranged from 0 to 0.03 m/s with a variable period, and the depicted flow fields represents the average velocities.

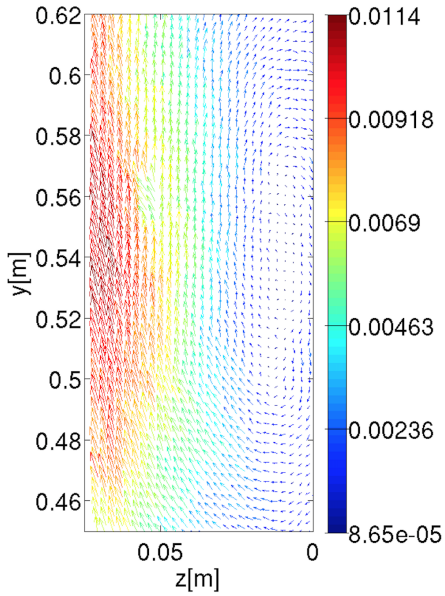

(a) Clockwise rotation

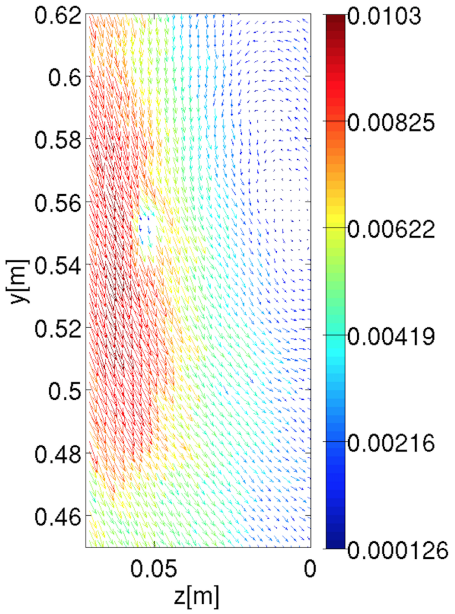

(b) Counter-clockwise rotation

Figure 5.4: Convection cell rotating clockwise (a) and counter-clockwise (b) during steady state. Magnitude of velocity ranges from 0.01 m/s (red) to 0 m/s (dark blue).

In Grafsrønningen and Jensen [2014], the assumption for obtaining a mean velocity field at every 5 minute interval during cool down, was that the mean flow didn't change during the period of time in which PIV measurements were carried out. The mean velocity field at each interval was found through averaging, and compared to RANS simulations averaged over the same time window. To further improve the experimental dataset, averaging was also performed over several consecutive runs. The periodic mean flow in the current experiment was expected to make these assumption invalid. An attempt was made to relate the period of the mean velocity to the period of the temperature data, but without success due to low temporal resolution in the velocity data. However, considering how the temperature fluctuations were caused by convective heat transfer, their periods were expected to be similar. In that case, the mean velocity would have an average period shorter than the time frame in which PIV measurements were carried out, and could therefore not be assumed constant. This was confirmed through visual inspection.

5.1.1 Error analysis

If one is to ensemble average over consequent runs in order to obtain the mean flow field, it is crucial that the experiment is repeatable. In this section, the repeatability of both the thermal and the kinematic flow field is investigated.

5.1.1.1 Repeatability of temperature measurements

The repeatability of the experiment was first scrutinized in terms of temperature measurements. Data from three consecutive cool down experiments were compared, and the repetition error was found for all sensors with the following formula:

$$\zeta_{1,2}(s) = \frac{\sum_{n=0}^{N-1}(T_1(s,t_n) - T_2(s,t_n))^2}{\sum_{n=0}^{N-1}(T_1(s,t_n))^2} \tag{5.1}$$

$$\zeta_{1,3}(s) = \frac{\sum_{n=0}^{N-1}(T_1(s,t_n) - T_3(s,t_n))^2}{\sum_{n=0}^{N-1}(T_1(s,t_n))^2} \tag{5.2}$$

where $T_l(s,t_n)$ contains temperature time series from 3 different runs $l = 1,2,3$, for sensors $s = 1,2,3,...,11$. This procedure was also carried out for the inclined pipe, and the resulting repetition errors are listed for each sensor in table 5.1. The standard deviation during steady state circulation is also listed for each sensor.

5.1.1.2 Repeatability of velocity measurements

The periodicity of the velocity field was believed to reduce the repeatability of the experiment. A comparison of steady state velocity data from three consecutive runs was conducted in the same manner as for the temperature measurements(see Eq. 5.1 - 5.2). Velocity data was filtered assuming CW and CCW rotation, and the mean in both categories was found through averaging. Figure 5.5 illustrates the vertical mean velocity profile at $y = 0.5m$ for the CW and the CCW rotation from 3 different steady state experiments. The velocity profiles during CW and CCW rotation are nearly symmetric around zero, explaining how the average velocity from all samples gave velocities close to zero for each run. The repetition error in vertical velocity during steady state for a horizontal pipe arrangement was found to be 4%. Repeatability during cool down is discussed in section 6.5.1

Table 5.1: Experimental repetition error for both horizontal and inclined pipe arrangement. The error was calculated based on Eq. (5.1)-(5.2) for all temperature sensors. Standard deviation of each sensor is also listed.

Sensor-position	**Repetition error** [%]		**Standard deviation** [$^{\circ}C$]	
	Horizontal	Inclined	Horizontal	Inclined
PT1	0.007	0.006	0.013	0.015
PT2	0.007	0.006	0.011	0.014
PT3	0.006	0.006	0.077	0.077
PT4	0.006	0.005	0.058	0.061
PT5	0.035	0.052	0.311	0.323
PT6	0.028	0.056	0.342	0.328
t3	0.079	0.123	0.283	0.188
t2	0.066	0.029	0.145	0.154
t1	0.045	0.034	0.208	0.209
k1	0.01	0.005	0.026	0.017
k2	0.008	0.005	0.066	0.054

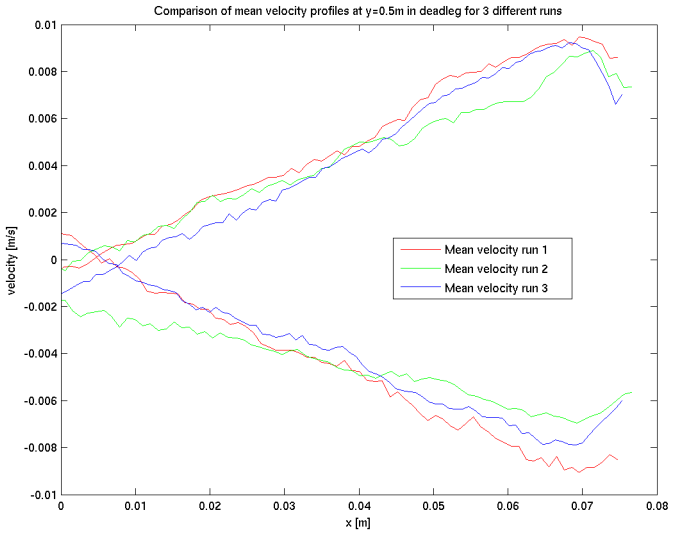

Figure 5.5: Vertical mean velocity at $y = 0.5m$ during 3 different steady state experiment for both CW and CCW rotation.

5.2 Numerical analysis

As mentioned in chapter 2, turbulent flow is very sensitive to grid resolution close to a solid boundary, and wall functions can be used in high-Re flow to reduce computational cost. However, when simulating turbulent natural convection at low-Re numbers, these wall functions are not valid, and it is crucial to avoid them. A near wall resolution of $y^+ < 2$ is recommended when using a $k-\omega$ SST model (ANSYS [2013a]) in order to avoid transition to wall functions. Figure 5.6 shows how this requirement was met for all solid-fluid interfaces during cool down. During steady state, the threshold of $y^+ < 2$ was exceeded only in the high-Re parts of the geometry, where the use of wall functions could be justified.

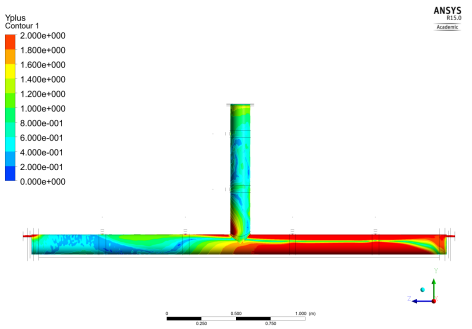

(a) y^+ during steady state

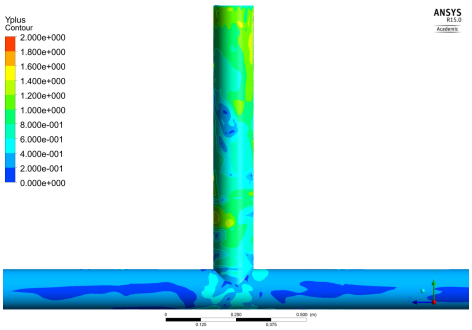

(b) y^+ during cool down

Figure 5.6: Wall functions were avoided by ensuring a $y^+ < 2$ during cool down. The colorbar ranges from blue to red, indicating $y^+ \approx 0$ and $y^+ > 2$ respectively.

5.3 Experiments vs CFD: Temperature

In this section the numerical output from several simulations is compared to the experimental data. Three attempts at modelling the boundary condition on top of the cold spot were made; constant temperature, external heat transfer coefficient, and heat flux. A comparison of experimental and numerical temperatures is presented for all these cases. The best suited boundary condition is used for simulating an inclined pipe in parameter study 1,and compared to experimental data. In parameter study 2, the experiment was modified to add water during cool down for both the horizontal and the inclined pipe arrangement. Temperatures from these experiments are compared to results from the previous numerical simulations.

5.3.1 Steady state simulations

Results from steady state simulations were used as initial conditions for the cool down simulations, and the accuracy of these simulations is therefore reported in table 5.2. Plus and minus indicate that the numerical model under- and over-predicted the temperatures respectively. The error was found to be negligible in the header, both internally and externally, whereas it was significant in the dead-leg. The maximum error here ranged from 13% to 25% for the 3 cool down cases, and fluctuations in temperature of ± 0.3°C was a common feature in both numerical and experimental results. Therefore, errors below ± 0.6°C(two standard deviations) could be explained by the physical behaviour of the flow in this area. However, errors below two standard deviations(Tab. 5.1) was only achieved in the header.

Table 5.2: Expermiental vs. CFD: error in initial temperature from steady state simulations

Sensor-	**Isothermal** $4°C$		**EHTC**		**Heat flux**	
name	Error $[°C]$	[%]	Error $[°C]$	[%]	Error $[°C]$	[%]
PT1	0.004	0.015	-0.033	0.137	0.046	0.192
PT2	0.043	0.179	0.009	0.036	0.084	0.349
PT3	0.035	0.149	-0.072	0.304	0.086	0.36
PT4	0.045	0.189	-0.095	0.399	0.089	0.376
PT5	-1.599	7.549	-1.42	6.703	-1.34	6.327
PT6	-2.336	11.662	-2.765	13.805	-1.255	6.265
t3	-0.352	2.056	-0.832	4.865	0.25	1.46
t2	1.27	6.822	0.95	5.104	1.758	9.442
t1	3.06	18.414	1.334	8.028	4.17	25.091
k1	0.559	2.408	0.567	2.444	0.617	2.659
k2	0.646	2.793	0.658	2.845	0.789	3.412

5.3.2 Cool down 1: Isothermal 4°C

An isothermal temperature condition was set on the entire top surface of the aluminium lid in the numerical model, imitating the experimental condition. Figure 5.7 illustrates the discrepancies between numerical and experimental water temperatures. In this figure, $\Delta T = T_{water} - T_{ambient}$ is plotted for 120 minutes of cool down. The initial error ranged from 0.015% in the header(PT1) to 11.6% in the dead-leg(PT6)(Tab. 5.2). The data coincided for approximately 40 minutes in the header (Fig. (a)-(d)), and 30 minutes in the dead-leg(Fig. (e)-(f)). After this, the numerical results showed an excessive cooling compared to experimental measurements. The amplitude of temperature fluctuations was also different as it decayed with time in the experiment, but not in the simulation(fig. (e)-(f)).

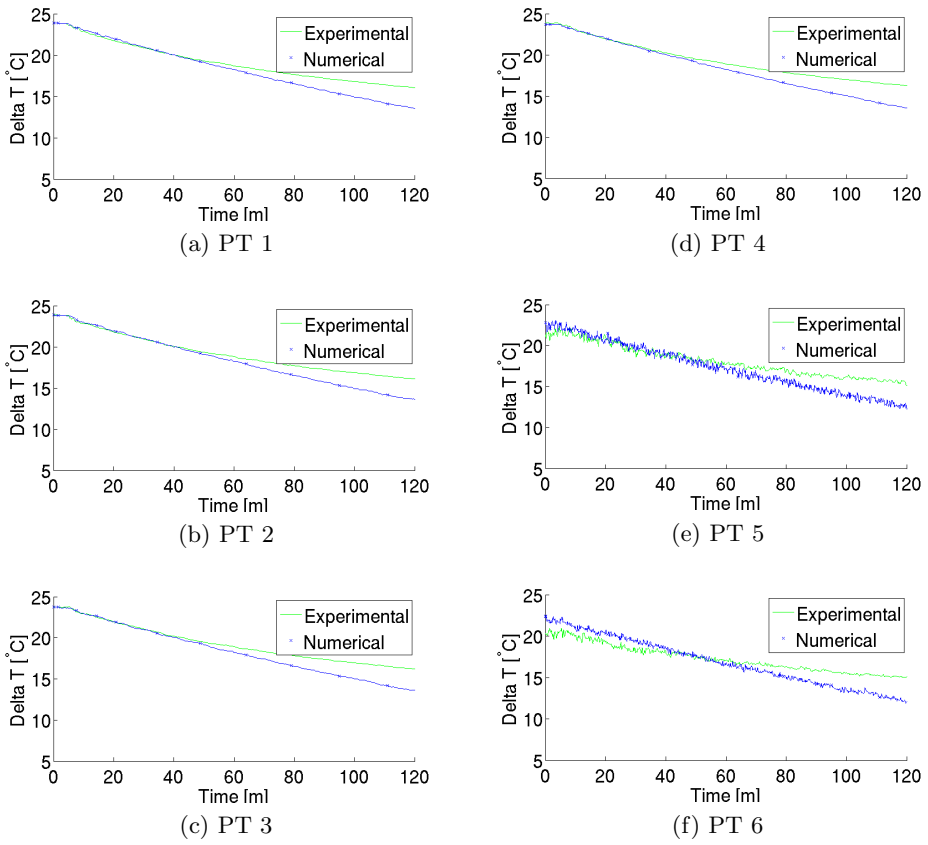

(a) PT 1 (d) PT 4

(b) PT 2 (e) PT 5

(c) PT 3 (f) PT 6

Figure 5.7: **Cool down 1** - Experimental vs. CFD - water temperature during cool down with constant **4°C** on cold spot

The cool down curves for the wall thermocouples are depicted in figure 5.8. Both the experimental and the numerical temperature data are given as ΔT between the plexiglass wall and the surrounding air. Initial error range from 2.4% in the header(k1 and k2), to 18.4% on top of the dead-leg(t1), exceeding the error in water temperature. In analogy with the observations for internal sensors, excessive cooling can be seen in the numerical results after about 40 minutes(figure (d) and (e)).

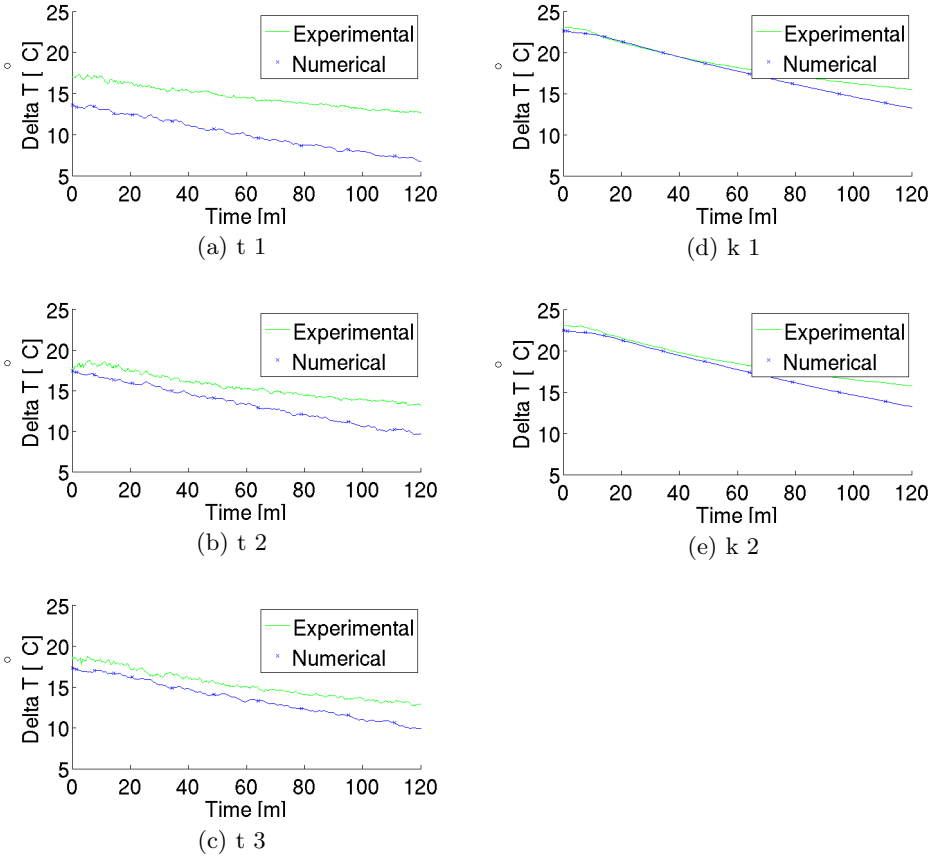

(a) t 1 (d) k 1

(b) t 2 (e) k 2

(c) t 3

Figure 5.8: **Cool down 1** - Experimental vs. CFD - plexiglass wall temperature during cool down with constant **4°C** on cold spot

5.3.3 Cool down 2: EHTC based on analytical correlation

An external heat transfer coefficient from the cold spot to the surrounding 4°C water was set. A comparison of experimental and numerical water temperatures($\Delta T = T_{water} - T_{ambient}$) is depicted in Fig. 5.9 for 3 hours of cool down. Numerical cooling rates were under-predicted during the first hour, and over-predicted the last two hours. The initial error was largest in the dead-leg, where it ranged from 6.7% on the bottom to 13.8% on the top. The amplitude of the numerical temperature fluctuations was too low during the first 40 minutes, and too high the remaining 140 minutes(Fig. 5.9(e)-(f)). Even though this simulation was unable to correctly predict the thermal field, the final temperature was actually pretty accurate. Thermal validation of a numerical model should therefore not be based on the error in final temperature alone, but on the entire process.

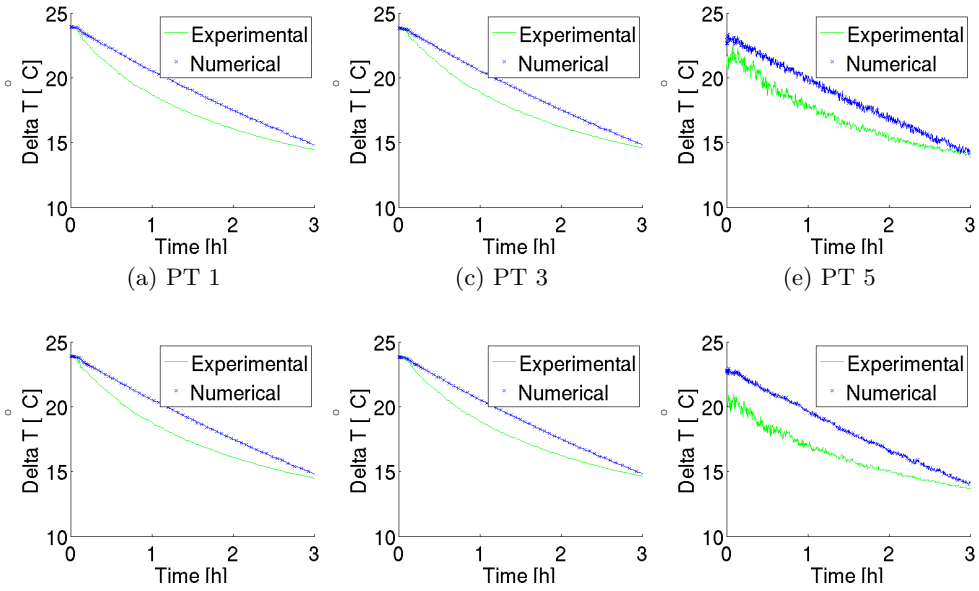

(a) PT 1 (c) PT 3 (e) PT 5

(b) PT 2 (d) PT 4 (f) PT 6

Figure 5.9: **Cool down 2** - Experimental vs. CFD - water temperature during cool down with **EHTC** on cold spot

The experimental and numerical temperature differential ΔT between the plexiglass wall and the surrounding air, is plotted for 3 hours of cool down in figure 5.10. The observations concerning prediction of cooling rates can be seen to apply also here. Nevertheless, the error in initial temperature was actually reduced compared to Cooldown 1, especially on top of the dead-leg(t1).

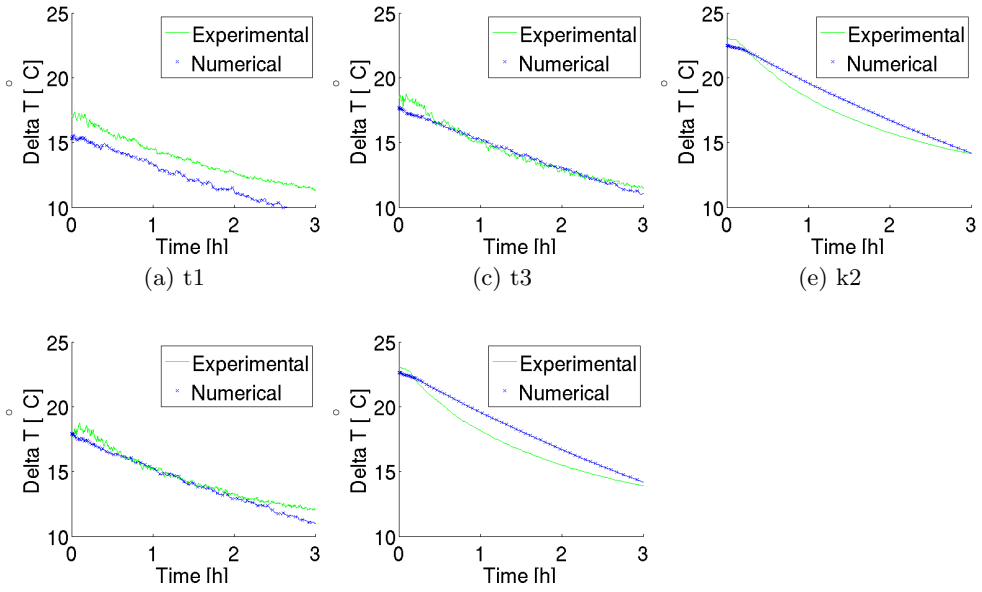

(a) t1 (c) t3 (e) k2

(b) t2 (d) k1

Figure 5.10: **Cool down 2** - Experimental vs. CFD - plexiglass wall temperature during cool down with **EHTC** on cold spot

5.3.4 Cool down 3: Heat flux from experimental data

In this section, the results from specifying the experimentally measured heat flux as a boundary condition on the cold spot wall in the numerical model is presented. All data is given as ΔT between the measurement point and the surrounding air during 1 hour of cool down. Figure 5.11 illustrates how experimental and numerical cooling rates coincided for all internal sensors, even after 40 minutes. However, the amplitude of the temperature fluctuations were over-predicted in the simulation. Compared to Cool down 1, some reduction was seen in the initial error on top of the dead-leg, but the error in the header was increased.

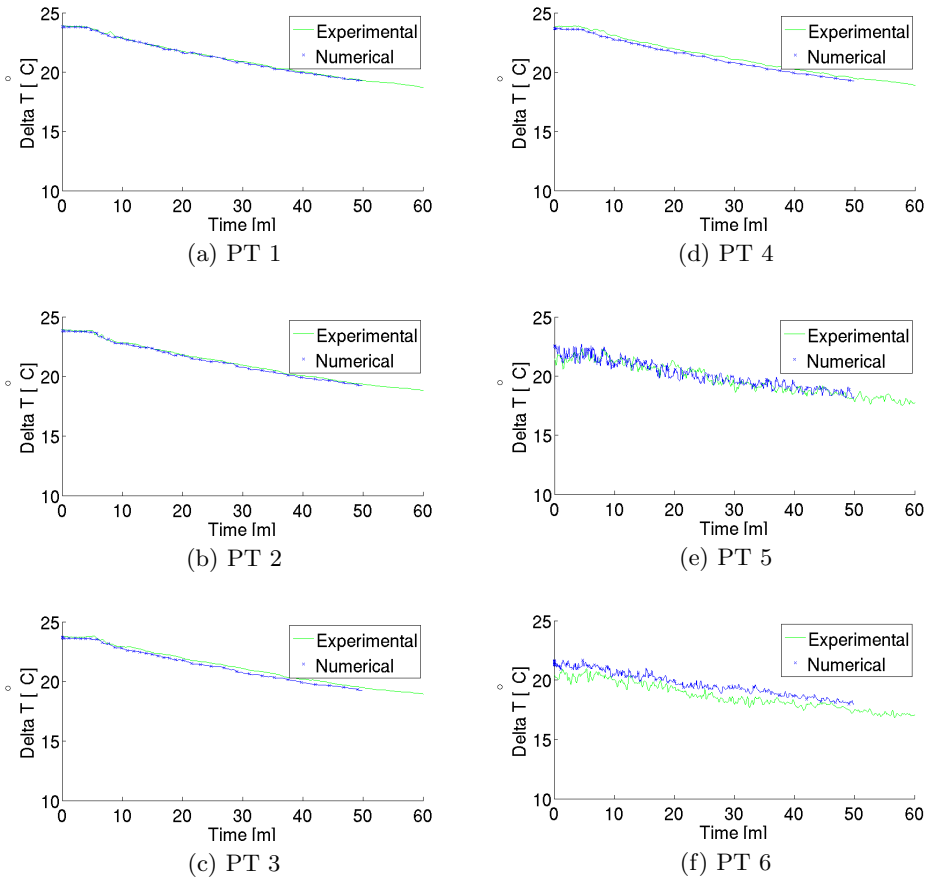

(a) PT 1 (d) PT 4

(b) PT 2 (e) PT 5

(c) PT 3 (f) PT 6

Figure 5.11: **Cool down 3** - Experimental vs. CFD water temperature during cool down with **heat flux** on cold spot

In figure 5.12, experimental and numerical cool down curves for the plexiglass wall are compared. It is evident, that an underestimation of numerical temperatures is still prevailing. The largest error is found on top of the deadleg(t1), where it is 25%. Compared to the first 40 minutes of Cooldown 1, the error in the header was increased.

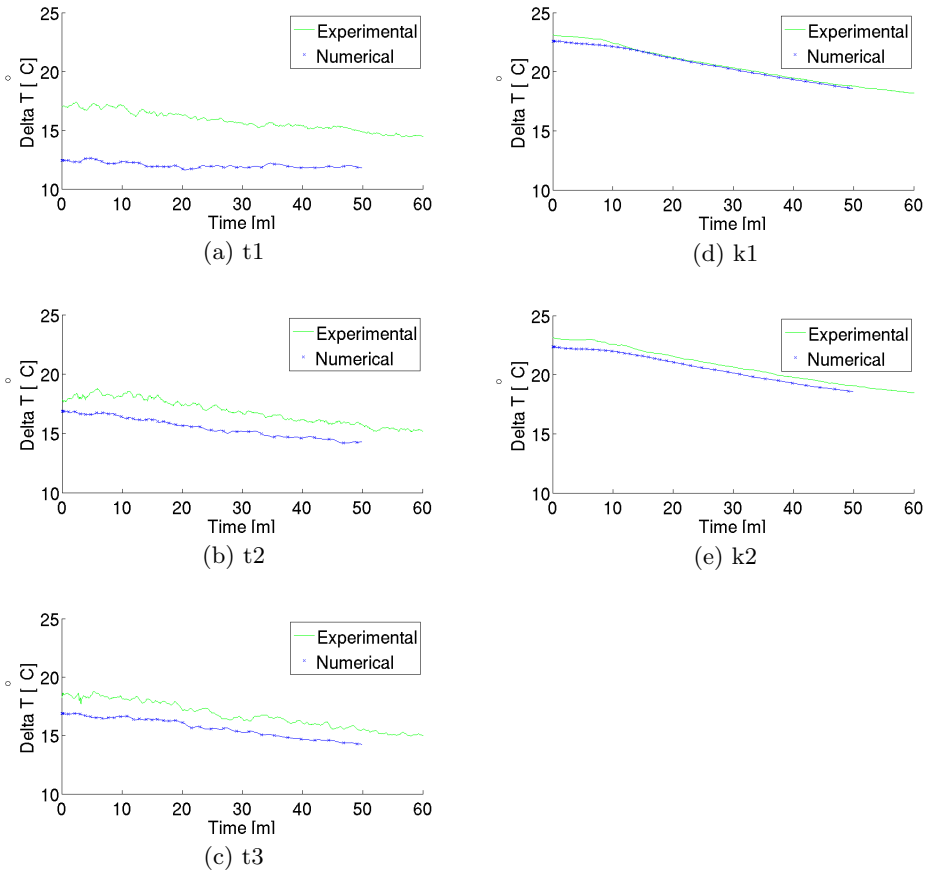

Figure 5.12: **Cool down 3** - Experimental vs. CFD - plexiglass wall temperature during cool down with **heat flux** on cold spot

5.3.5 Parameter study: Cool down P1

In this section, the results from the first parameter study(P1) are presented. An inclination of 2.4° was created by elevating the downstream side of the table, and the results are compared to the main experiment in Fig. 5.13. The inclination can be seen to increase the cooling effect in the upstream part of the header(a). It also caused the temperature to fluctuate downstream in the header(b).

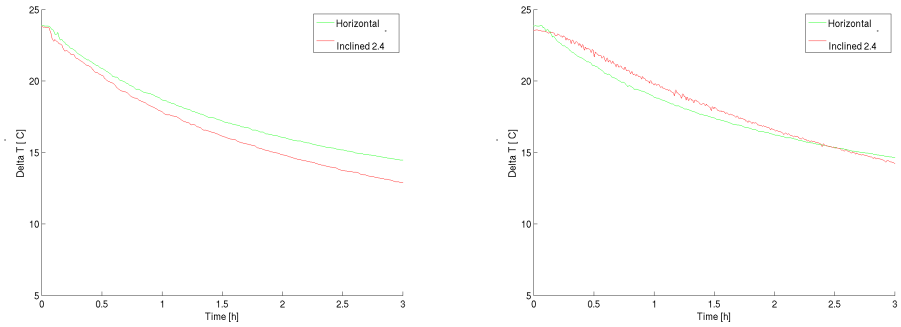

(a) PT 1 (b) PT 4

Figure 5.13: **P1** - comparison of experimental temperature data for horizontal and inclined pipe

Based on the results from the previous 3 cool down simulations, an isothermal 4°C boundary condition was considered the best modelling approach during the first 30-40 minutes. This boundary condition was therefore used for simulating the pipe with an inclination of 2.4°. In Figure 5.14, experimental and numerical temperatures are compared for PT6 in the dead-leg, and PT4 in the header. As already mentioned, temperature fluctuations now appeared in the header(a) as well as in the dead-leg(b). The experimental and numerical results departed from each other after 30 and 40 minutes in the dead-leg and header respectively. The remaining cool down curves for water temperatures are given in the appendix(figure A.2), and they all show good agreement with experimental data during the initial 30-40 minutes, as with the horizontal case. Cool down curves for wall thermocouples are also given in the appendix(figure A.3).

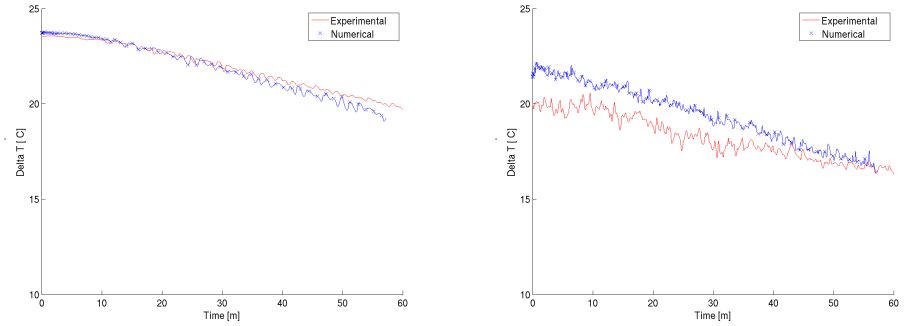

(a) PT 4 (b) PT 6

Figure 5.14: **P1**- Experimental vs. CFD - water temperature during cool down with **4° C** on cold spot

5.3.6 Parameter study: Cool down P2

In Cool down 1, it was shown that there is a trend for the numerical and experimental data to start disagreeing after 30 minutes. It was necessary to figure out if this was caused by compressibility effects which were not modelled in CFX. In parameter study 2 (P2), the top valve was opened up to a water reservoir for both horizontal and inclined pipe and temperatures were measured during cool down. To evaluate if the addition of water during cool down had an effect on temperatures, measurements were compared to data from the main experiment. The comparison is plotted in figure 5.15. After about 30 minutes, the cool down curves in the dead-leg started deviating, whereas the same effect was seen approximately 10 minutes later in the header. It was shown that the effect was actually an isolating vacuum layer which accumulated on top of the dead leg in the experiment, preventing heat exchange due to convection between water and the cold spot. This effect was not modelled in CFX, proving that it was indeed the reason for the disagreement between numerical and experimental results in Cool down 1. Experimental temperature data were now believed to coincide with data from Cool down 1, and the cool down curves are given on page 56.

In parameter study 1 it was shown that a small inclination made temperatures in the header lower by $2°C$ after 3 hours of cool down. Physical observations revealed that this was due to a delay in time for the vaccum layer to cover the entire cold spot surface when the pipe was inclined. Therefore, the increased cooling rate depicted in figure 5.13(a), disappeared when continuously adding water. This is shown in Fig.5.16(a), where cool down curves from an horizontal and inclined pipe arrangement with water addition is compared. The only place where cool down behaviour changed

significantly due to the inclination alone, was in the downstream part of the header. After 3 hours, the temperature in this part was actually 1.5°C higher when the pipe was inclined (figure 5.16 (b)). The trend for the experimental and numerical data to start disagreeing after 30 minutes was also seen when the pipe was inclined(Fig.5.14). With the compressibility effects now removed, this disagreement was believed to vanish, and another attempt at benchmarking the inclined numerical model is given on page 58.

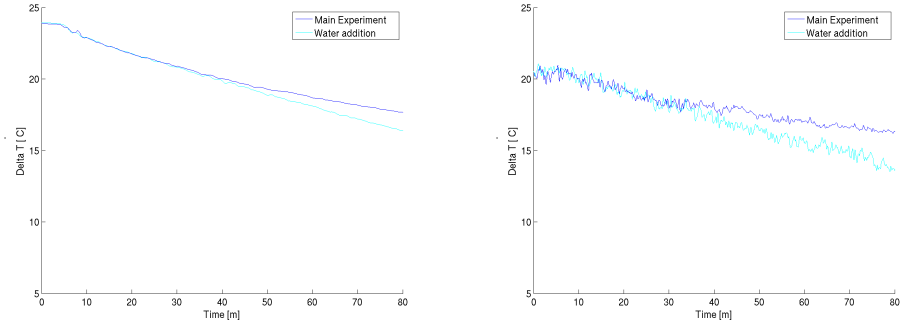

(a) PT 1 (b) PT 6

Figure 5.15: **P2vsMain**- Comparison of experimental temperature data for **horizontal** pipe arrangement in header(a) and dead-leg(b), with and without water addition

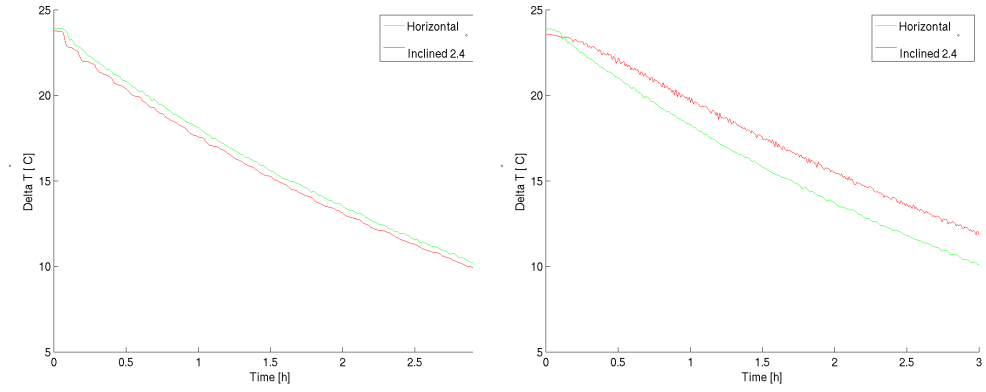

(a) PT 1 (b) PT 4

Figure 5.16: **P2** - comparison of experimental temperature data for horizontal and inclined pipe with top valve connected to water reservoir

Experimental vs. CFD: Horizontal pipe

Adding water during the cool down experiment was shown to be the key to obtain an experiment fit for benchmarking a numerical model. Experimental data now coincided well with CFD data from Cool down 1, even after 40 minutes. In figure 5.17, internal temperature data can be seen to agree with numerical results for the duration of 3 hours. The errors in initial temperature were the same as in Cool down 1, and are listed in table 5.2.

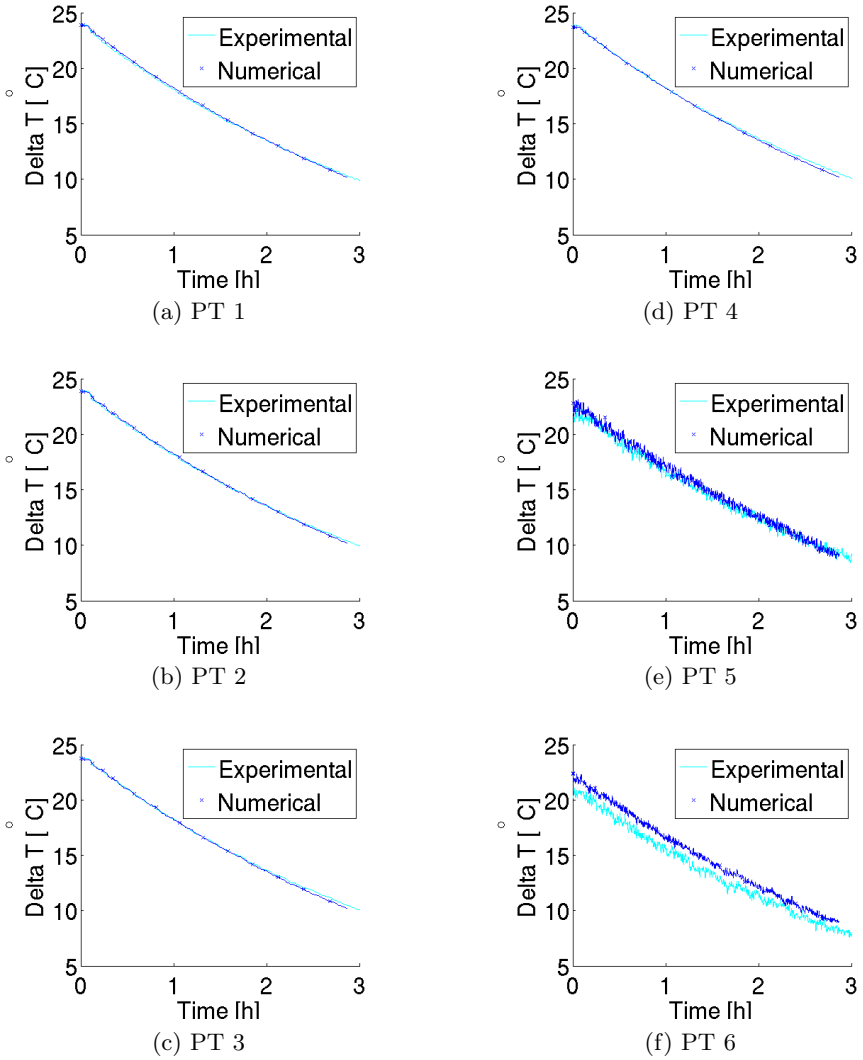

(a) PT 1 (d) PT 4

(b) PT 2 (e) PT 5

(c) PT 3 (f) PT 6

Figure 5.17: **P2 horizontal** - Experimental vs. CFD - water temperatures during cool down with **4**° on cold spot

Experimental and numerical cooling rates for the wall sensors also agreed well for 3 hours as illustrated in Fig. 5.18. However, the numerical model still under-predicted the initial temperatures, leading to the constant errors listed in table 5.2.

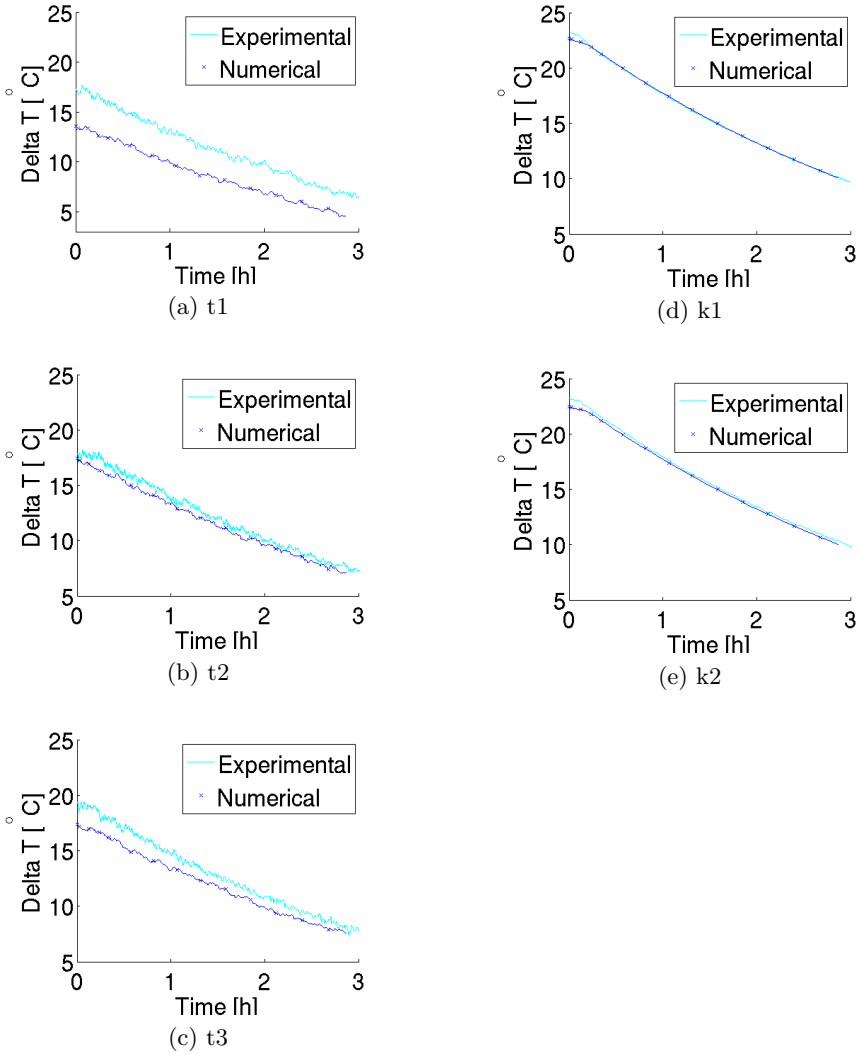

(a) t1 (d) k1

(b) t2 (e) k2

(c) t3

Figure 5.18: **P2 horizontal** - Experimental vs. CFD - plexiglass wall temperatures during cool down with **4°** on cold spot

Experimental vs. CFD: Inclined pipe

With the compressibility effects removed from the experiment, a comparison of experimental and numerical temperature data is given in this section for the inclined pipe. In figure 5.19, cool down curves can be seen to coincide for all internal temperature sensors in the header for 1 hour, with the exception of PT4. This was believed to be caused by compressibility effects accumulating also in this elevated part of the header. However, it did not seem to have an effect at the other measurement locations. Temperatures in the dead-leg were still over-predicted.

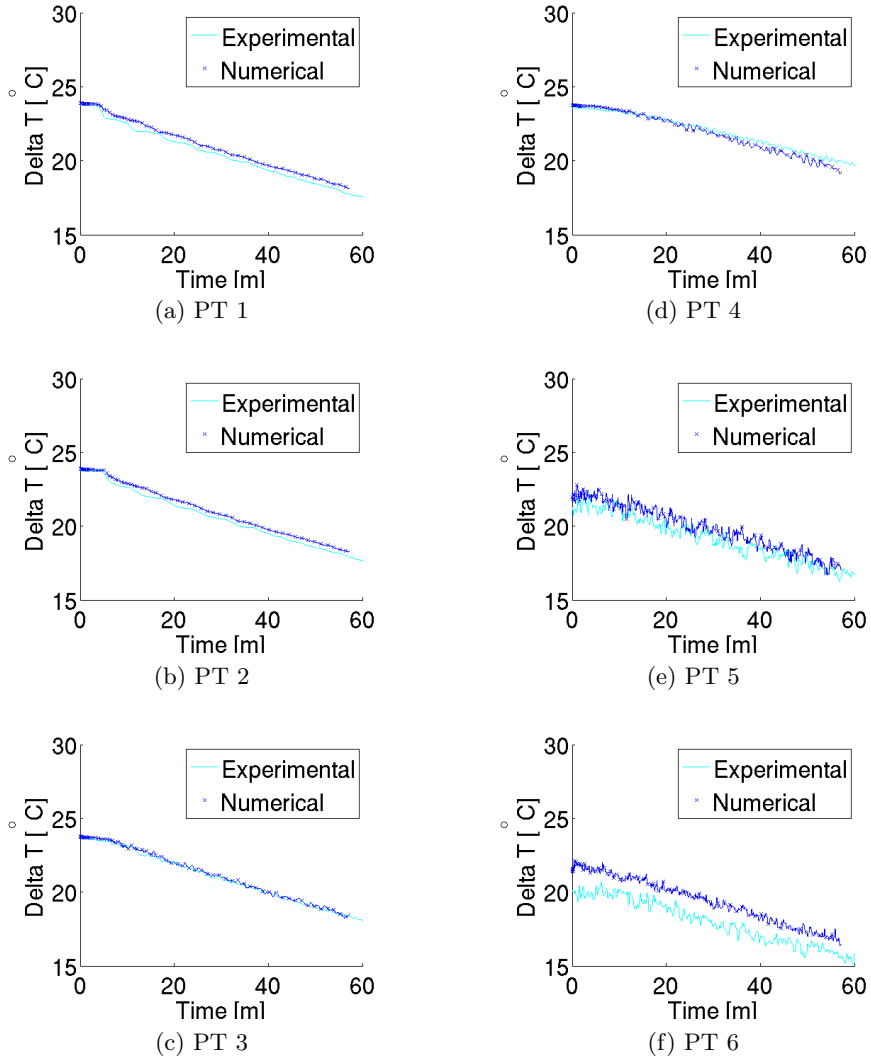

(a) PT 1 (d) PT 4

(b) PT 2 (e) PT 5

(c) PT 3 (f) PT 6

Figure 5.19: **P2 inclined** - Experimental vs. CFD - water temperature during cool down with **4°** on cold spot

Cool down curves for the plexiglass wall temperatures are given in Fig. 5.20. Experimental wall temperatures agreed well with numerical results in the header for 1 hour, with the exception of an initial error from steady state simulations. As with the horizontal case, cooling rates in the dead-leg were similar, but with a constant error in temperature ranging from 7 to 20 % at the bottom and top of the dead-leg respectively.

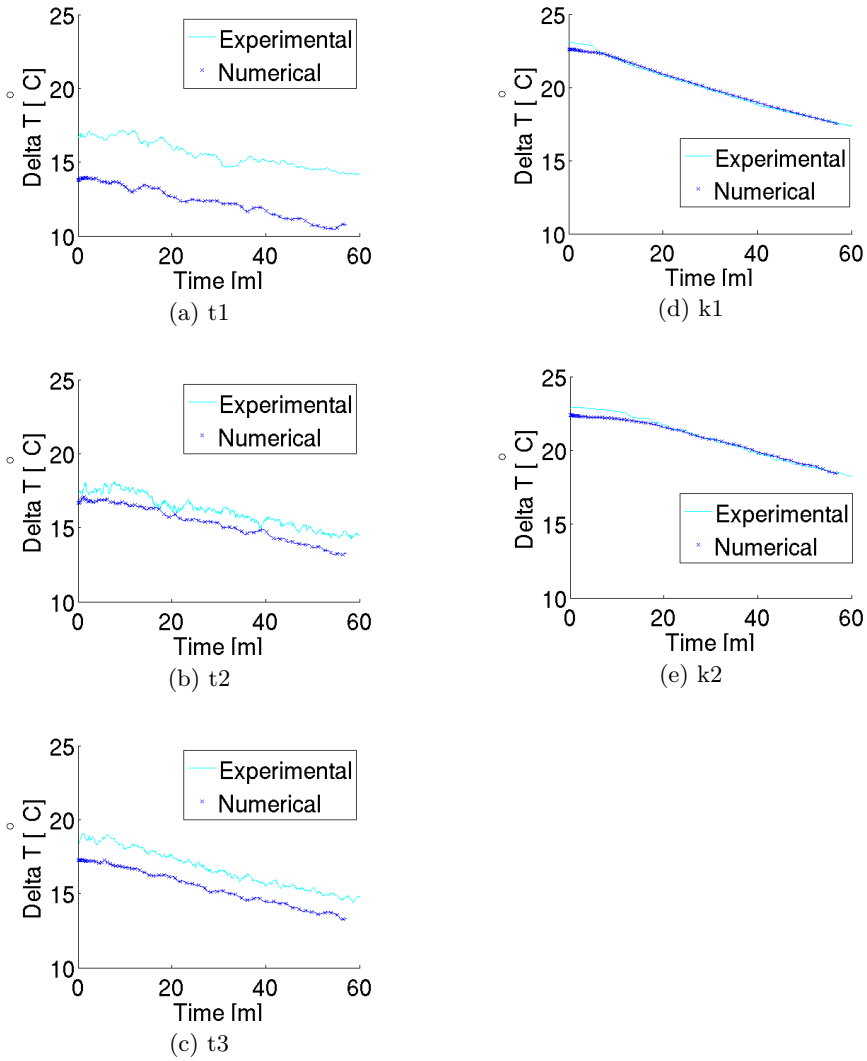

(a) t1 (d) k1

(b) t2 (e) k2

(c) t3

Figure 5.20: **P2 inclined** - Experimental vs. CFD - plexiglass wall temperatures during cool down with **4°** on cold spot

5.4 Experiments vs. CFD: Velocity

In the previous section, three different approaches to modelling the cold spot were assessed. As shown in figures 5.7 and 5.8, the error in temperature was found to be constant during the first 40 minutes, only to increase the last 140 minutes. This sudden change in cool down behaviour was further investigated in the parameter studies, resulting in a satisfactory match of experimental and numerical cool down curves. Velocities from the most plausible simulation(Cool down 1) will be compared to experimental velocities for the horizontal pipe in this section.

At every 5 minutes interval during a 3 hour cool down, 31 image pairs were obtained over a period of 186 seconds. From the steady state analysis, it was shown how the mean velocity field could be categorized into a convection cell with either clockwise(CW) or counter-clockwise(CCW) rotation direction. An attempt was made to use the same filtering technique during cool down, and compare the result with RANS velocities filtered likewise. The experimental data at the first 5 minute interval is given in table 5.3. In figure 5.21, the numerical and experimental velocity are compared for the first 30 minutes with the use of this filtering technique. Comparison shows that they both behave periodically with a CW and CCW rotation, but besides that they are not comparable.

Table 5.3: Velocity data at t=5 min during cool down. Distance from the wall is scaled with the pipe diameter $D = 0.143m$, while the velocity scale is $V_0 = \sqrt{g\beta\Delta TD}$

$\mathbf{z/D}$ [-]	$\mathbf{V^+/V_0}$ [-]	$\mathbf{V^-/V_0}$ [-]	$\mathbf{U^+/V_0}$ [-]	$\mathbf{U^-/V_0}$ [-]
0.0089	0.0188	-0.0191	0.0071	-0.0076
0.0338	0.0217	-0.0221	0.0053	-0.0033
0.0587	0.0234	-0.0187	0.004	-0.0012
0.1085	0.0252	-0.0144	0.0008	0.0011
0.1584	0.0243	-0.0093	0.0015	0.0045
0.2332	0.0184	-0.005	0.0015	0.0018
0.283	0.0112	-0.0058	-0.0007	0.0001
0.3329	0.0094	-0.0001	-0.0019	0.0035
0.3827	0.0047	0.0037	-0.0018	0.004
0.4325	0.0016	0.0093	-0.0059	0.0029
0.4824	-0.0008	0.0092	-0.0044	0.0044
0.5322	0	0.0085	-0.0031	0.0038

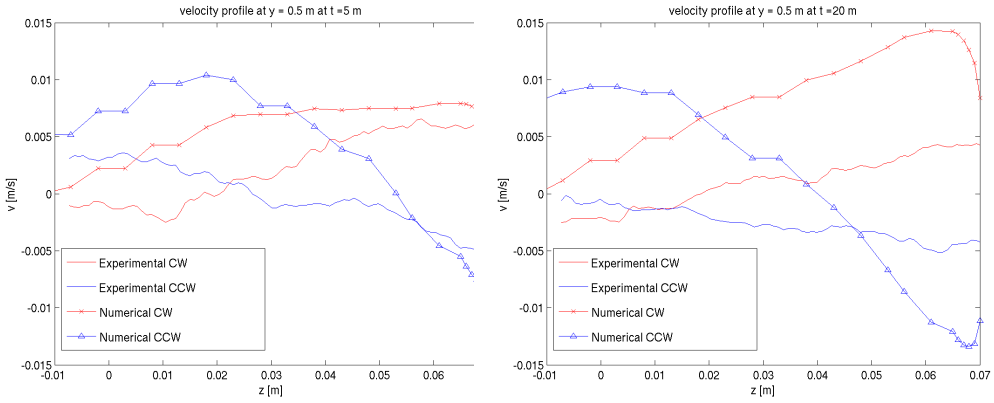

(a) 5 minutes

(d) 20 minutes

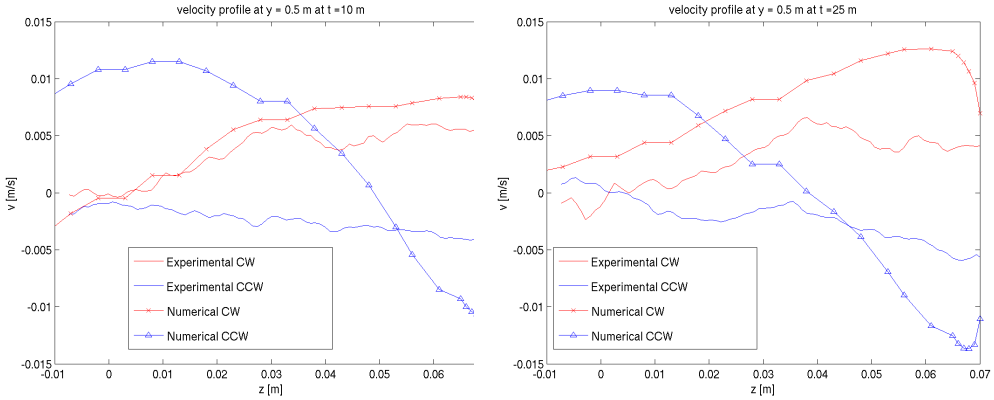

(b) 10 minutes

(e) 25 minutes

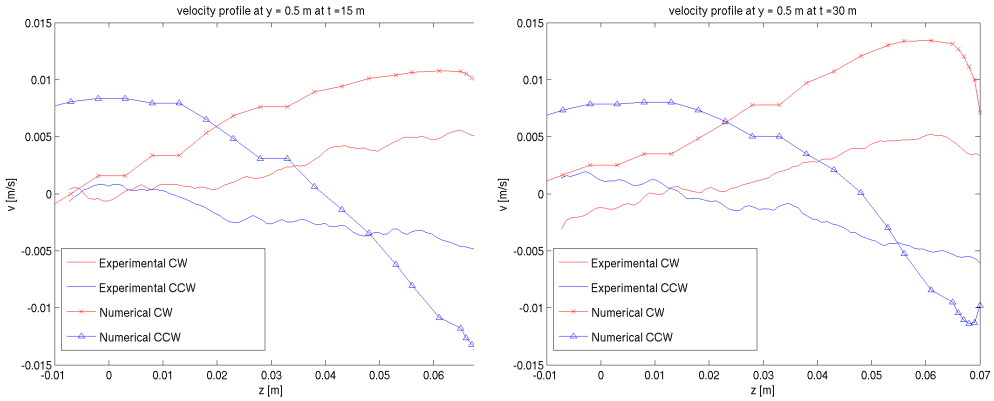

(c) 15 minutes

(f) 30 minutes

Figure 5.21: Cool down 1 - Experimental vs. CFD - mean vertical velocity profile at $y = 0.5m$ during the first 30 minutes of cool down for both CW and CCW rotation

Comparing RANS velocities to mean velocities from PIV measurements was challenging due to the flow being both transient and periodic. In order to evaluate (dis)similarities in flow behaviour, the continuous RANS velocity was compared to the instantaneous experimental velocity at every 5 minutes interval. In figure 5.22, the velocity 1 mm from the wall at $y = 0.5m$ is plotted as a function of time. Both numerical and experimental velocities exhibit a periodic behaviour, and have approximately the same amplitude.

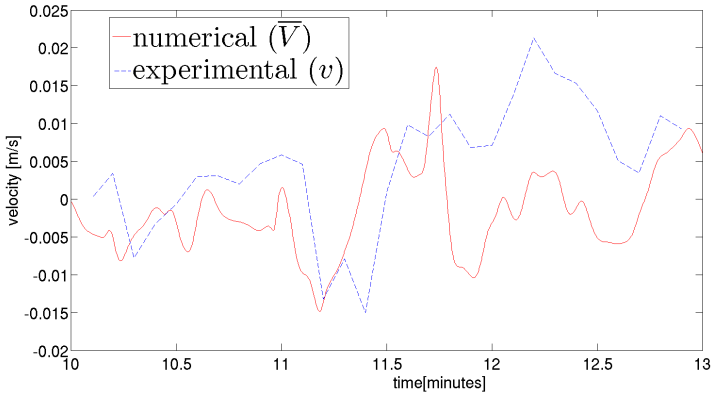

(a) 10 minutes

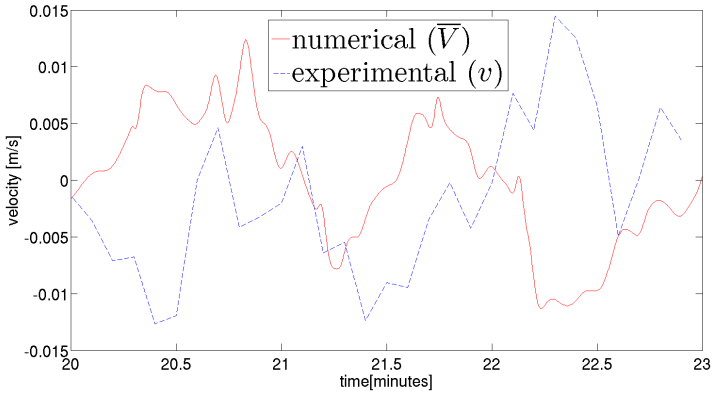

(b) 20 minutes

Figure 5.22: A comparison of RANS velocity and measured instantaneous velocity in the dead-leg as a function of time during cool down: $y = 0.5m$ and $z = 0.0705m$

Deviations in the experimental data from a purely periodic behaviour(see figure 5.22) was assumed to be caused by turbulence. Usually, fluctuating components could have been filtered out by ensemble averaging over consecutive experiments, but this would have required the periodicity in the velocity field to be repeatable. The repeatability of velocity measurements during a 3 hour cool down was investigated for 3 different runs at 5 minute intervals. In figure 5.23, velocity data for $y = 0.5m$ and $z = 0.0705m$ is plotted against time. The velocity measurements exhibit similar amplitudes, but it is difficult to perform any averaging since all runs show different phase behaviour.

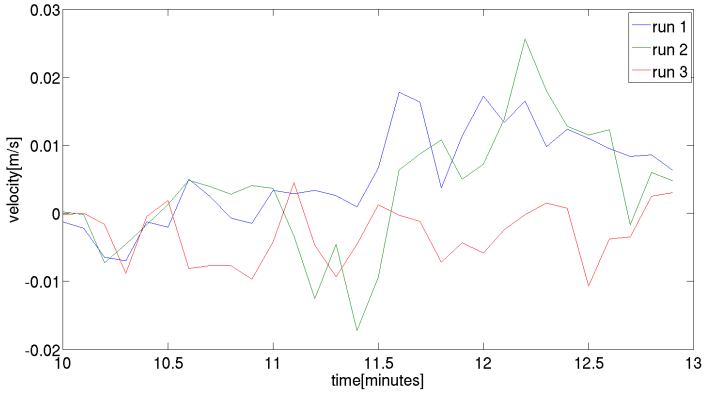

(a) 10 minutes

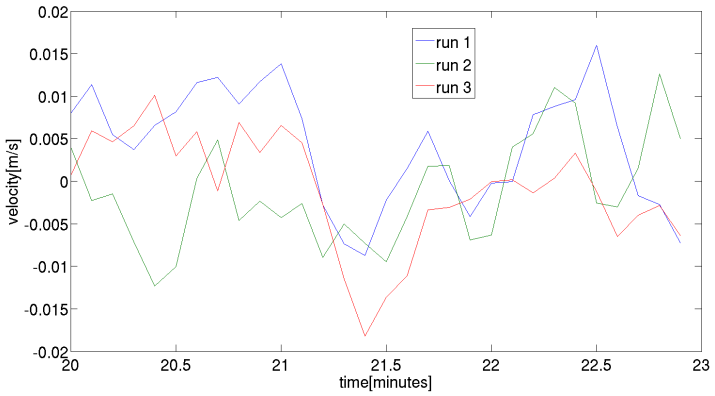

(b) 20 minutes

Figure 5.23: Repeatability of vertical velocity from 3 consecutive runs: $y = 0.5m$ and $z = 0.0705m$

Chapter 6

Conclusion

In this section, the results presented in the previous chapter will be discussed, and the suggestions for further research will be presented.

6.1 Main findings

In the previous study by Grafsrønningen and Jensen [2014], cool down experiments over 3 hours were conducted on a water filled T-shaped plexiglass pipe, representing a production header with a vertical dead-leg. The header was insulated, while the dead-leg was kept uninsulated. It was shown that cool down simulations were more sensitive to mesh design than choice of turbulence model. Mesh independent results were obtained by running a series of mesh convergence tests. The thermal field was correctly predicted with a RANS model for the entire cool down, even though the flow was laminar after 60 minutes. Velocities in the dead-leg coincided well with experimental PIV data during the first 60 minutes, but RANS was not able to predict laminar flow kinematics. In the present study, the experiment was modified with a cold spot on top of the dead-leg, and a more uniform insulation on the header. These modifications were also made in the numerical geometry, and a mesh was created based on the recommendations given by Grafsrønningen and Jensen [2014] in Workbench. The addition of a cold spot changed the experiment in the following way:

- After 3 hours of cool down, temperatures in the header were lower by 9°C.
- The flow field was dominated by three dimensional large scale convection cells

- These convection cells set up a periodic mean flow field, rotating clockwise and counter clockwise

Despite the increased complexity, simulations in CFX using a $k-\omega$ SST turbulence model have successfully predicted the thermal field for the duration of 3 hours. Correct prediction of temperatures was also achieved when the header was inclined by 2.4° for 1 hour of cool down. The RANS simulations failed to recreate the periodic mean velocity field observed in the experiment, but had the same amplitude and similar oscillating character.

Three different approaches to modelling the cold spot was assessed: isothermal wall, external heat transfer coefficient(EHTC), and heat flux. It has been shown that the simplest case, namely an isothermal boundary condition, yielded the best results for internal temperatures. Specifying the exact heat flux through the cold spot surface based on experimental measurements, did not improve accuracy for internal temperatures, nor lower the error in wall temperature. Setting a semi-analytically obtained EHTC showed some improvement on wall temperature accuracy, but failed to predict the cooling rate leading to erroneous internal temperatures.

This thesis also describes technical approaches to performing a full scale cool down tests when the component contains a cold spot. In section 5.3.2 it was shown how important volume reduction due to increased density of water can be for the overall heat loss during cool down. In this study, physical observations revealed an isolating vacuum layer on top of the dead-leg, which prevented heat exchange due to convection between water and the cold spot after 35 minutes, leading to a rapid drop in overall cooling rate. It was therefore not possible to use the dataset to validate the numerical model at this stage(since such effects were not modelled in CFX). Only when compensating for volume reduction by adding water during cool down, was it possible to match numerical and experimental cool down curves(section 5.3.6). In full scale cool down tests, the pipe materials are rarely transparent, and these effects should be considered up front. The following recommendations are given when designing such experiments:

- Avoid situating the cold spot on top of the geometry. The effect of compressibility will not prevent benchmarking of numerical results if it is not accumulated in vicinity of the cold spot.
- If the cold spot is situated on top of the geometry, water should be added during cool down to facilitate benchmarking.

It should be noted that vacuum was also created in the elevated part of the header for the inclined experiment. However, this was an insulated area,

and the effect was only seen locally around the PT4 sensor.

The difficulties with obtaining mean velocities when dealing with a periodic 3 dimensional decaying mean flow was assessed. At every 5 minute interval during cool down, 31 velocity fields were obtained over a time frame of 186 seconds, providing a temporal resolution of 6 seconds. The experiment was repeated several times with the intention of ensemble averaging over consecutive runs. However, the periodicity in the velocity data was not repeatable with the current technique, limiting the validity of this approach. An attempt was made to sort the mean flow for each run into a clockwise and counter-clockwise rotation, perform averaging separately within each category at every 5 minute time interval, and finally average over consecutive runs. This proved challenging because of the low temporal resolution(6 seconds between each image pair), making it difficult to distinguish large scale trends from random fluctuations. According to the Nyquist Theorem, it would not be possible to measure any trend of less than 12 seconds with the current set-up. On top of all these issues, the flow was decaying with time, making it hard to justify a time average over the 186 seconds.

Mesh quality and choice of turbulence model were not considered as sources of error in this thesis. In the previous study by Grafsrønningen and Jensen [2014], $k-\omega$ SST was recommended as the best suited turbulence model, and mesh independent solutions were acquired through using the mesh sizing presented in table 4.1. The only error sources considered in this thesis are:

- Numerical boundary condition error
- Experimental measurement error

Heat transfer from the horizontal and the vertical cylinder was modelled with the use of an external heat transfer coefficient. Correlations for Nusselt numbers on these geometries have been the topic of many research papers, and were therefore not considered as a source of error. External heat transfer through cold spots have not received as much attention in research papers, and there were no known correlations for modelling it. In the numerical model, an isothermal $4°C$ wall was considered the best modelling approach, and it was defined symmetrically on the external surface. However, the experimental boundary condition was not so symmetric. On its way across the aluminium lid, water was heated by $1.53°C$ during steady state. The geometry of the channels transporting the water was also believed to create local temperature gradients(see appendix B for geometry of the lid).

Measuring internal temperatures with a PT element is considered an accurate procedure as long as the specific offset has been found for each sensor. The error in wall temperature should also be negligible when averaging over

data from 3 sensors at each position. Discrepancies in cool down curves were therefore not believed to be caused by measurement errors.

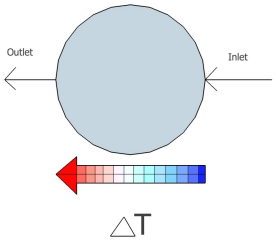

Figure 6.1: Gradient across the surface area of the aluminium lid. During steady state circulation it was found to be $\Delta T = 1.53°C$.

6.2 Further Recommendation

Based on the findings in this thesis, the following recommendations are given in order to improve the experiment:

1 Improve the temporal resolution of PIV data by using a high speed, high resolution camera with direct data transfer to a hard drive. This could make it easier to separate large scale trends from small scale trends, revealing the "true" periodic mean velocity field.

2 Reduce the gradient across the cold spot by increasing the pump flow rate through the lid. This would require an external pump since the cooler pump in the current experiment was already at maximum capacity.

If the above experimental improvements are made, the following recommendations are given on numerical strategy:

1 Perform simulations using LES with an isothermal wall as boundary condition on the cold spot. This could enable direct comparison with experimental velocity data for both period and amplitude of the large scale convection cells.

2 If unsuccessful, perform a number of sensitivity simulations to obtain the correct EHTC, or modify the numerical model to include the entire cold spot geometry as sketched in appendix A.

Bibliography

Inc. ANSYS. *ANSYS CFX-Solver Modeling Guide*, 2013a.

Inc. ANSYS. *ANSYS CFX-Solver Theory Guide*, 2013b.

A. A. Ayati, J. Kolaas, A. Jensen, and G. W. Johnson. A piv investigation of stratified gas-liquid flow in a horizontal pipe. *International Journal of Multiphase Flow*, 61:129–143, 2014.

Adrian Bejan and Shiego Kimura. Experimental study of natural convection in horizontal pipe with different end temperatures. *Internal Journal of Heat and Mass Transfer*, 23:1117–1126, 1980.

P.L. Betts and I.H. Bokhari. Experiments on turbulent natural convection in an enclosed tall cavity. *International Journal of Heat and Fluid flow*, 21:675–683, 2000.

S.W. Churchill and H.H.S. Chu. Correlating equations for laminar and turbulent free convection from a horizontal cylinder. *International Journal of Heat and Mass Transfer*, 18:1049–1053, 1975.

P.A. Durbin and B.A. Pettersson Reif. *Statistical Theory and Modeling of Turbulent Flows, Second Edition.* John Wiley & Sons, Ltd, The Atrium, Southern Gate, Chichester, West Sussex, United Kingdom, 2011.

Stig Grafsrønningen. *Numerical and experimental investigation of natural convection from horizontal heated cylinders.* PhD thesis, University of Oslo, 2012.

Stig Grafsrønningen and Atle Jensen. Cool down simulatons of subsea equipment. *CFD in Oil & Gas, Metallurgical and Process Industries*, 10, 2014.

M. A. Habib, H. M. Badr, S. A. M. Said, E. M. A. Mokheimer, I. Hussaini, and M. Al-Sanaa. Characteristics of flow field and water concentration in a horizontal deadleg. *International journal of Heat and Mass transfer*, 41:315–326, 2005.

Dwight Janoff, Nigel McKie, Janardhan Davalath, and FMC Energy Systems. Prediction of cool down times and designing of insulation for subsea production equipment. Offshore Technology Conferencen, Houston Texas 3-6 May, 2004.

J. Kolaas, A. Jensen, and J. K. Sveen. *Optimization of PIV parameters using synthetic images of fluctuating flow with non-zero mean velocity.* PhD thesis, University of Oslo, 2014.

Uduak A. Mme. *Free convection flow and heat transfer in pipe exposed to cooling.* PhD thesis, Norwegian University of Science and Technology, 2010.

Omega. *The Omega Complete Temperature Measurement Handbook and Encyclopedia.* Omega Engineering Inc., 1987.

B.A. Pettersson Reif. Advanced turbulence modeling and theory. Lecture notes, 2014.

Johan Kristian Sveen and Edwin A. Cowen. *Quantitative Imaging Techniques and Their Application to Wavy Flows, In PIV and Water Waves.* World Scientific, ISBN 981-238-914-8, 2004.

S. Tian and T. G. Karayiannis. Low turbulence natural convection in an air filled square cavity. *International journal of Heat and Mass transfer*, 43: 867–884, 2000.

Frank M. White. *Viscous Fluid Flow, Third Edition.* McGraw-Hill, 1221 Avenue of the Americas, New York, 2006.

W. M. Yan and T. F. Lin. Theoretical and experimental study of natural convection pipe flows at high rayleigh number. *International Journal of Heat and Mass Transfer*, 34:291–303, 1991.

Appendix A

Additional plots and figures

The cold spot geometry is given in figure A.1. Dimensions in the figure are in mm, R and Ø refer to radius and diameter respectively. Thickness of the bottom plate was 2 mm, and 18 mm for the entire plate including the channel walls. Initially, the mid section of this geometry(without the bottom plate) was printed out with a 3D printer, attached to a 2 mm aluminium plate on the bottom, and finally sealed with plexiglass on the top. However, the plastic turned out to be leaking, and the choice was therefore to use an end mill to create the bottom and middle section as one aluminium piece. Aluminium was chosen due to its high thermal conductivity, and availability.

The additional cool down curves from parameter study 1 is given in figure A.2 and A.3.

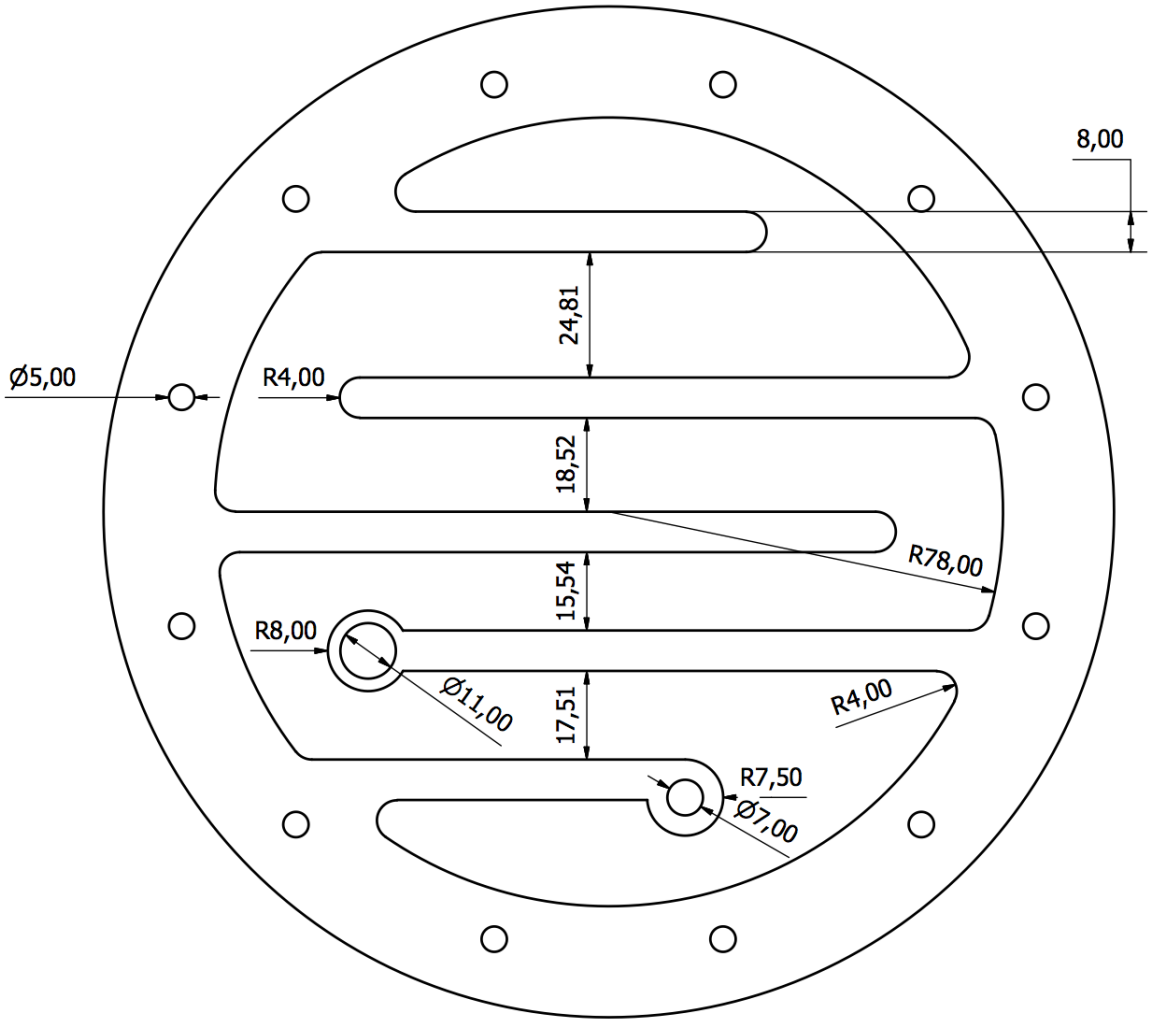

Figure A.1: Geometry of cold spot

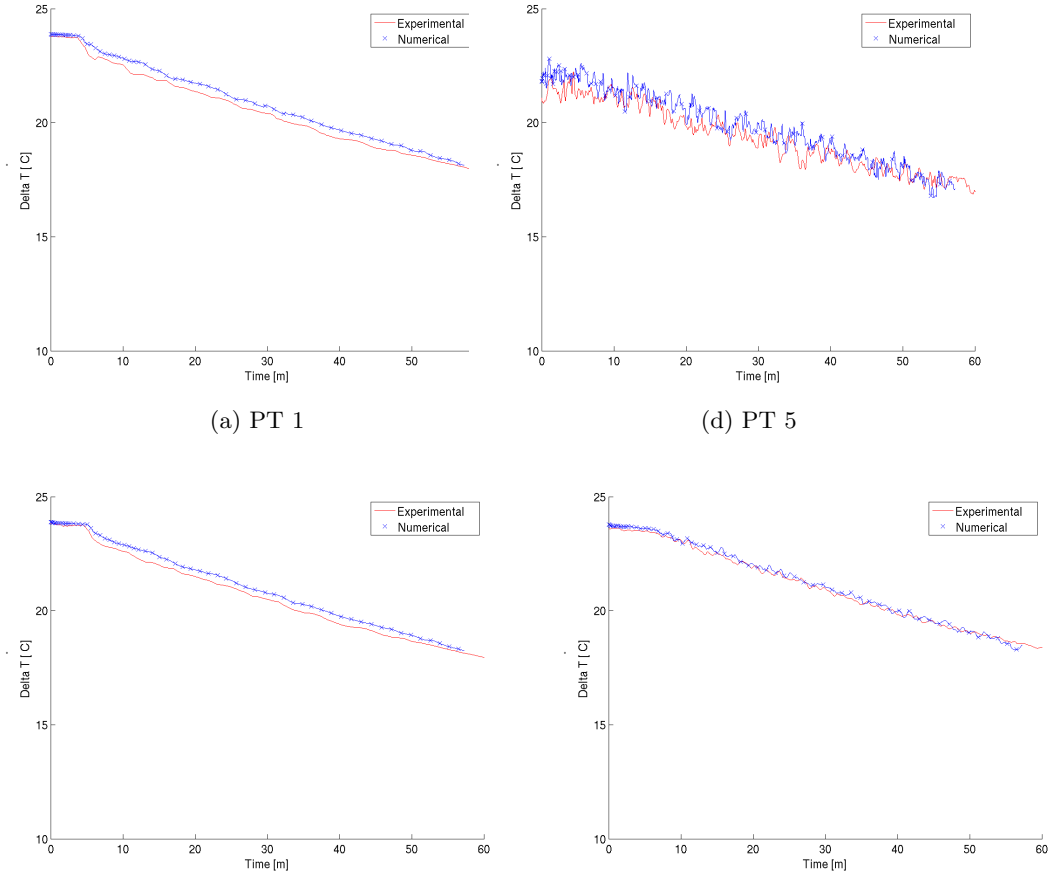

(a) PT 1

(d) PT 5

(b) PT 2

(c) PT 3

Figure A.2: **P1**- Benchmark vs. CFD data for internal temperature sensors during 1 hour cool down with **4**° on cold spot

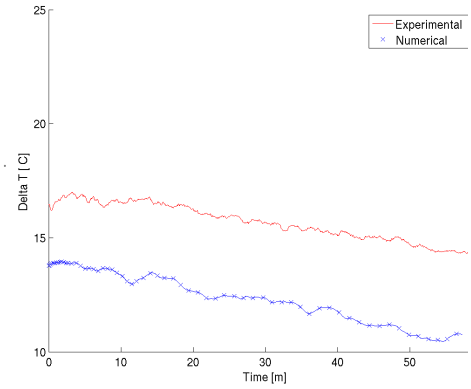

(a) t1

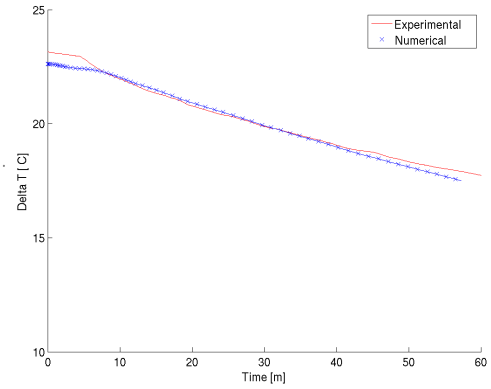

(d) k1

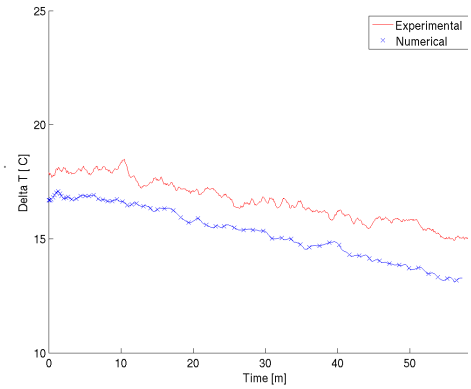

(b) t2

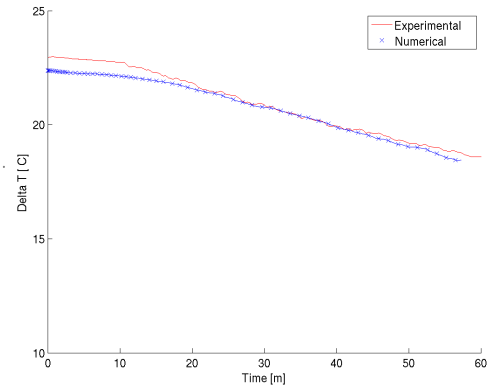

(e) k2

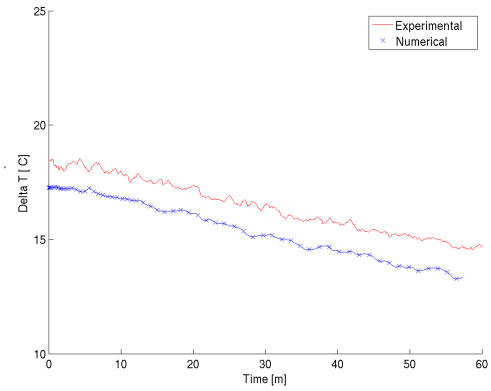

(c) t3

Figure A.3: **P1**- Benchmark vs. CFD data for wall thermocouples during 3 hour cool down with **4**° on cold spot

Appendix B

Organisation of experimental and numerical data

All the data is stored in reference with the date it was obtained, and they are organised as shown below.

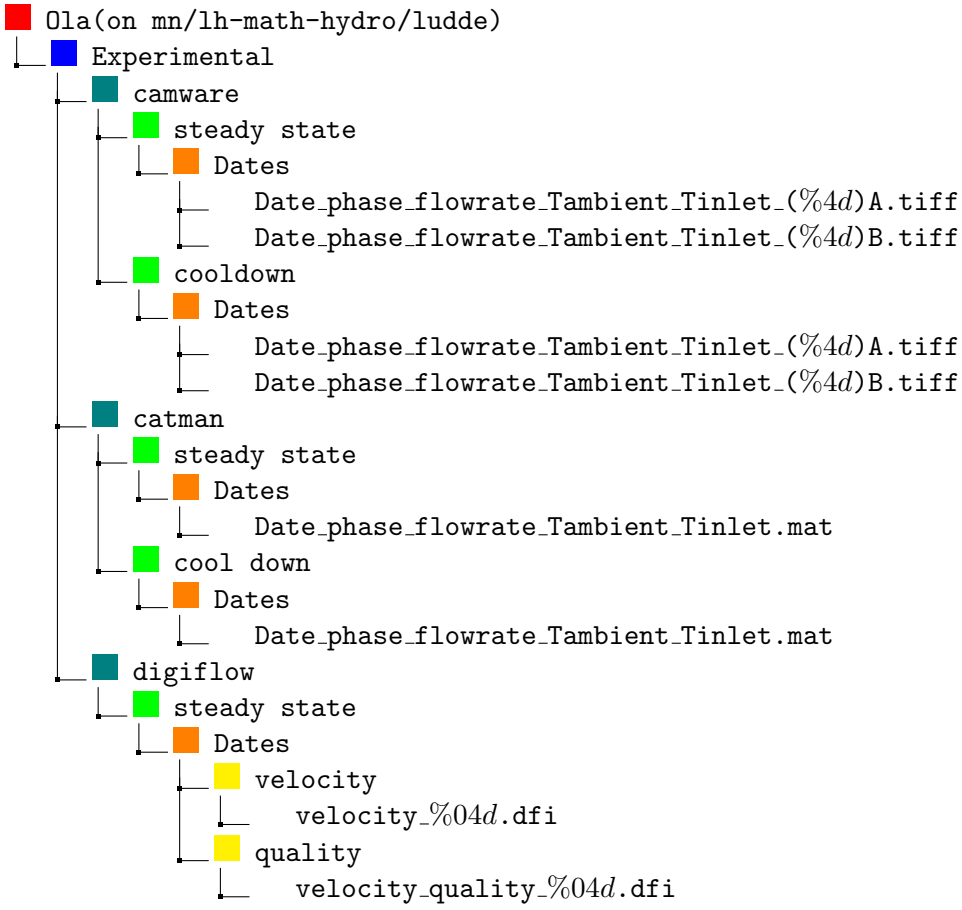

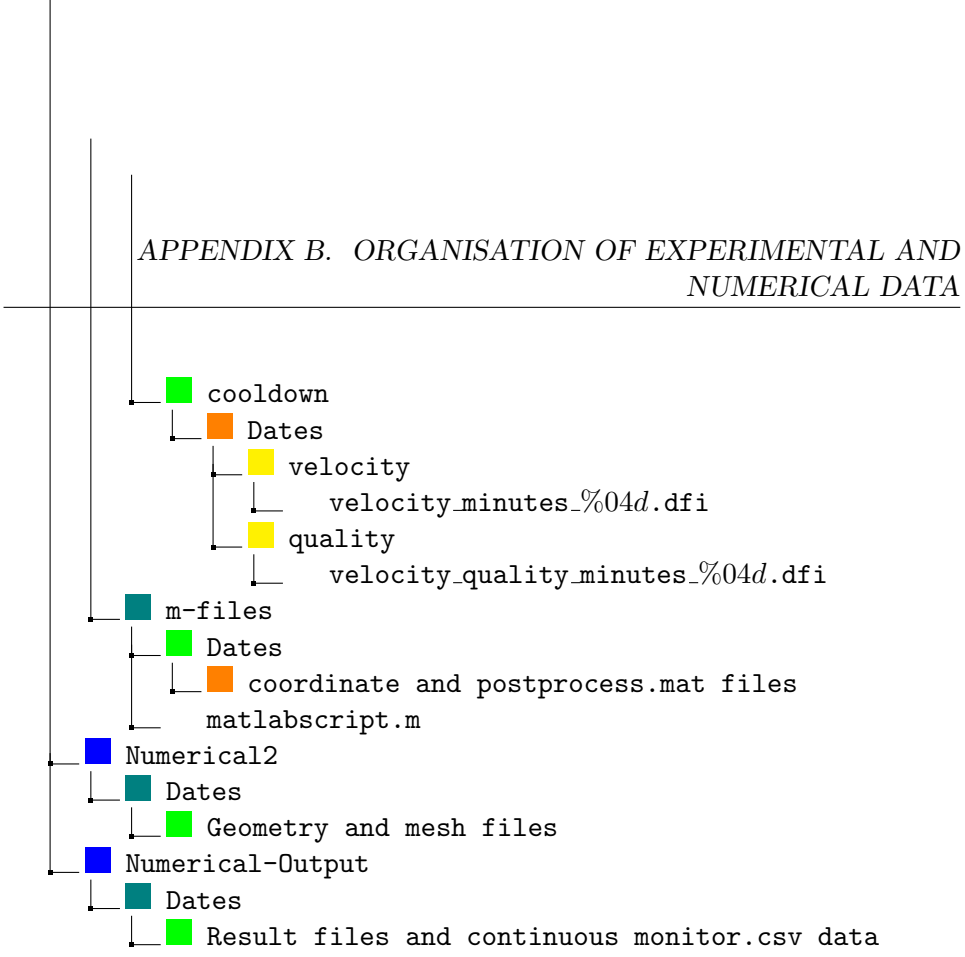

A short description of what type of experiment/simulation was conducted on these dates is given below.